

Strong hole-photon coupling in planar Ge for probing charge degree and strongly-correlated states

Franco De Palma^{1,2†}, Fabian Oppliger^{1,2†}, Wonjin Jang^{1,2†}, Stefano Bosco^{3,4}, Marián Janík⁵, Stefano Calcaterra⁶, Georgios Katsaros⁵, Giovanni Isella⁶, Daniel Loss³, Pasquale Scarlino^{1,2*}

¹Hybrid Quantum Circuit Laboratory, Institute of Physics and Center for Quantum Science and Engineering, École Polytechnique Fédérale de Lausanne (EPFL), Lausanne, 1015, Switzerland.

²Center for Quantum Science and Engineering, École Polytechnique Fédérale de Lausanne (EPFL), Lausanne, 1015, Switzerland.

³Department of Physics, University of Basel, Klingelbergstrasse 82, Basel, 4056, Switzerland.

⁴QuTech, Delft University of Technology, Delft, The Netherlands.

⁵Institute of Science and Technology Austria, Am Campus 1, Klosterneuburg, 3400, Austria.

⁶L-NESS, Physics Department, Politecnico di Milano, via Anzani 42, Como, 22100, Italy.

*Corresponding author(s). E-mail(s): pasquale.scarlino@epfl.ch;

†These authors contributed equally to this work.

Abstract

Semiconductor quantum dots (QDs) in planar germanium (Ge) heterostructures have emerged as front-runners for future hole-based quantum processors. Here, we present strong coupling between a hole charge qubit, defined in a double quantum dot (DQD) in planar Ge, and microwave photons in a high-impedance ($Z_r = 1.3 \text{ k}\Omega$) resonator based on an array of superconducting quantum interference devices (SQUIDs). Our investigation reveals vacuum-Rabi splittings with coupling strengths up to $g_0/2\pi = 260 \text{ MHz}$, and a cooperativity of $C \sim 100$, dependent on DQD tuning. Furthermore, utilizing the frequency tunability of our resonator, we explore the quenched energy splitting associated with strong Coulomb correlation effects in Ge QDs. The observed enhanced coherence of the strongly correlated excited state signals the presence of distinct symmetries within related spin functions, serving as a precursor to the strong coupling between photons and spin-charge hybrid qubits in planar Ge. This work paves the way towards coherent quantum connections between remote hole qubits in planar Ge, required to scale up hole-based quantum processors.

Keywords: Strong charge-photon coupling, Hole qubit, Quantum dot, cQED, Ge/SiGe heterostructure, Strong-correlation

1 Introduction

Semiconductor quantum dots (QDs) represent a promising platform for advanced quantum information processing [1–3]. Particularly, hole confinement in QDs enables rapid electric spin manipulation due to the large spin-orbit interaction [4–8]. QD-based hole qubit systems have been implemented in various platforms including fin field-effect transistors (finFETs) [9, 10], Ge/Si core/shell nanowires [5, 11], and planar Ge/SiGe heterostructures [4, 12, 13]. Among these, planar Ge stands out due to its exceptional characteristics [6], including high hole mobility ($\mu > 10^6 \text{ cm}^2\text{V}^{-1}\text{s}^{-1}$ [14]), low charge noise [15], and a low effective mass [16]. Furthermore, nuclear isotope purification can be performed, effectively mitigating magnetic field noise and enhancing the qubit coherence [6]. Building on all these advantages, recent works have demonstrated coherent single- and two-qubit operations [4, 13], scalable multi-qubit array architecture [12, 17], and coherent spin shuttling [18] in planar Ge.

In the context of circuit quantum electrodynamics (cQED), the hybridization of microwave photons in superconducting cavities with QD-based qubits holds enormous potential for various applications in quantum technology. These applications include enabling long-range interactions between distant quantum dot qubits [19–21], achieving rapid and high-fidelity charge and spin state detection [22, 23], as well as facilitating analog quantum simulation of open quantum systems [24], and advancing the development of gigahertz photodetectors [25]. However, achieving strong light-matter coupling is a fundamental prerequisite for these endeavors. While several previous experiments have successfully demonstrated strong coupling for electrons hosted in Si [26–28], GaAs [29, 30], InAs nanowires [31], and for holes in silicon nanowire transistors [32], the strong coupling of holes in planar Ge has remained elusive [33–35].

Previous hybrid cQED experiments primarily focused on resonators interacting with the ground and first excited states of double quantum dot (DQD) charge- or spin-two level systems. In fact, in typical QD structures, additional single-dot orbital states usually lie at energies higher than $100 h\cdot\text{GHz}$, making them inaccessible to microwave resonators [36]. However, low excitation energies can arise from Coulomb interaction-induced renormalization of orbital energies in single QDs, leading to the formation of strongly correlated states (SCSs) [37, 38]. When further enhanced by anisotropic QD confinement [39], these states can lead to excitation energies below $10 h\cdot\text{GHz}$ that have been observed in GaAs [40, 41], Si [42], and carbon nanotube [43, 44] QDs and attributed to Wigner molecular states [38, 45–50]. The emergence of SCSs is a general phenomenon, which can take place in QDs defined in any semiconductor platform [41–43]. Such SCSs have profound implications for quantum information processing, offering an encoding for spin-charge hybrid qubits based on exchange interaction [41, 47]. If not properly controlled, it can significantly reduce the fidelity of conventional readout schemes in spin qubits [39]. In Ge, it has been also shown that SCSs enable anomalous splittings of spin energy levels without the need for magnetic fields [51]. These findings suggest that low-lying SCSs could serve as a valuable interface between QD qubits and superconducting circuits in hybrid architectures.

In this study, we establish strong coupling between a microwave photon and a DQD-based hole charge qubit in a planar Ge/SiGe heterostructure, using a high-impedance frequency-tunable resonator based on superconducting quantum interference devices (SQUIDs) [30]. We explore different DQD configurations and achieve a charge-photon vacuum-Rabi splitting (charge decoherence rate) up to $2g_0/2\pi \sim 520 \text{ MHz}$ (down to $\Gamma/2\pi \sim 57 \text{ MHz}$). We estimate a system cooperativity of $C \sim 100$, among the highest reported for QDs charge-resonator hybrid systems to date [29]. Our device geometry facilitates formation of SCSs in Ge, unveiling a quenched energy spectrum of SCSs in the DQD. Leveraging the frequency tunability of the SQUID array resonator, we perform resonant energy spectroscopy of SCSs in the DQD and extract their energy spectra. By exploring several pairs of adjacent inter-dot configurations, we observe selective coupling to the resonator based on the parity of the DQD hole number and enhanced coherence times for certain excited SCSs, which we attribute to states with a different spin structure [41, 52].

2 Results

Architecture for hybrid circuit QED with holes in planar Ge

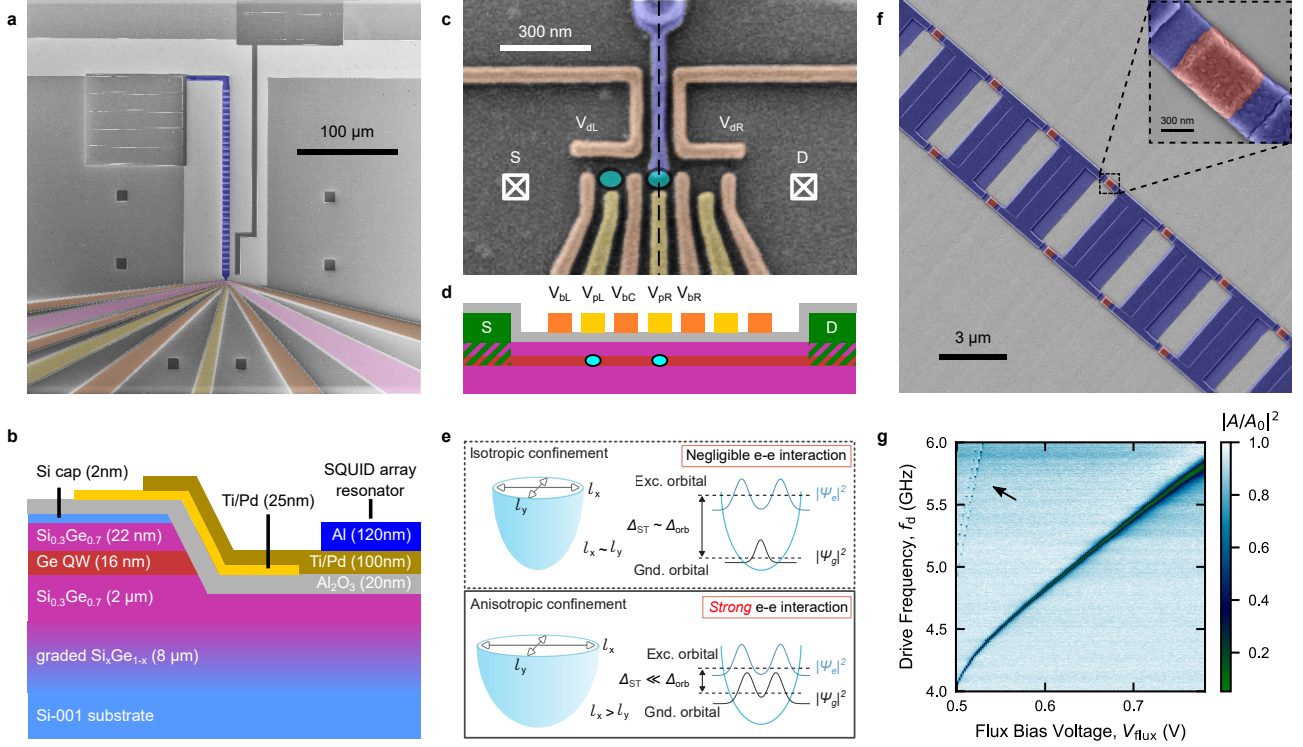


Fig. 1 Superconductor-semiconductor hybrid architecture on planar Ge heterostructure. **a**, False-colored scanning electron micrograph of a representative hybrid device. The SQUID array resonator (violet) is capacitively coupled to the transmission line on top. The QDs are defined electrostatically by barrier (orange) and plunger (yellow) gates. The Ge quantum well is etched away everywhere except for a small mesa region (pink) used to host the QDs. Ohmic contacts are patterned on the extensions of the mesa region. **b**, Schematic side-view of the heterostructure and the device across the black dashed line in **c**. **c**, False-colored scanning electron micrograph of the QDs region. The expected position of the DQD is highlighted by cyan ellipses. The plunger gate V_{pL} (V_{pR}) mainly controls the electrochemical potential of the left (right) QD, while V_{bL} (V_{bR}) modulates the tunnel coupling strength of the left (right) QD to left (right) reservoir. V_{bc} controls the inter-dot tunnel coupling strength t_c . **d**, Side-view of the device across the QD array. **e**, Schematic of the two-body ground and excited state wavefunctions (ψ_g and ψ_e) and single QD energy splitting for two different classes of QD confinement potential. Under isotropic confinement, the ground and excited state wavefunctions have distinct shapes, which result in large orbital splitting Δ_{orb} . In the anisotropic and strongly interacting case, the symmetry of ψ_g is broken, resulting in a quenched singlet-triplet splitting $\Delta_{ST} \ll \Delta_{orb}$ [39]. **f**, False-colored scanning electron micrograph of the SQUID array resonator. Inset: Zoom-in of a single Josephson junction (red). **g**, Flux tunability of the SQUID array resonator. Normalized amplitude of feedline transmission $|A/A_0|^2$ as a function of drive frequency f_d and bias voltage V_{flux} applied to the superconducting coil mounted perpendicularly to the sample (see Supplementary Note 1). Higher resonator modes are visible near the half-flux point (black arrow) [53]. The device is operated in a dilution refrigerator with a base temperature of 10 mK (see Supplementary Note 1).

Fig. 1a shows the hybrid superconductor-semiconductor device fabricated on a Ge/SiGe heterostructure [54]. As shown in Fig. 1b, the 16 nm Ge quantum well (QW), hosting the 2-dimensional hole gas (2DHG), is ~ 24 nm below the surface. A conductive channel, defined by selectively etching the Ge QW, hosts a DQD (cyan ellipses in Figs. 1c, d) defined by metallic gate electrodes. The gate layout of our device supports relatively large QDs (radius $l_{QD} \sim 70$ nm). The Wigner ratio $\lambda_W = E_{ee}/E_{orb} \propto l_{QD}$ (see Supplementary Note 6) quantifies the ratio between the Coulomb interaction strength ($E_{ee} \propto 1/l_{QD}$) and the orbital confinement energy ($E_{orb} \propto 1/l_{QD}^2$). Coulomb interactions become increasingly relevant in large QDs, as the ones studied here. In our experiment, we estimate $\lambda_W \sim 4.46$. Coulomb correlation renormalizes the energy of orbital states in QDs, thus quenching the orbital splitting and therefore the singlet-triplet splitting Δ_{ST} [37]. Furthermore, anisotropic QD confinement is expected to enhance the correlation effect and reduce Δ_{ST} even further (see Supplementary Note 6) [39], as illustrated in Fig. 1e. Orbital state renormalization induced by Coulomb correlation and confinement anisotropy is expected to significantly alter also the charge density distribution of the ground state, promoting the formation of Wigner molecular (WM) states (see Supplementary Figure 11) [39, 40, 42–44].

The right dot is coupled to the superconducting resonator (Fig. 1f) via the violet electrode in Fig. 1c (see Supplementary Note 1) [30]. This is designed to maximize the capacitive coupling by completely overlapping

one QD and, therefore, to efficiently couple to the DQD via transverse charge-photon interaction [26, 29, 30]. The resonator consists of an array of $N = 32$ SQUIDs (Fig. 1f) with an inductance of $L \sim 0.63$ nH/SQUID, resulting in an equivalent lumped impedance of $Z_r \sim 1.3$ k Ω [30]. The high-impedance resonator enhances the charge-photon coupling strength g_0 by maximizing the vacuum voltage fluctuation $V_{0,\text{rms}} = 2\pi f_r \sqrt{\hbar Z_r/2}$, according to the relation $g_0 = \frac{1}{2}\beta_r V_{0,\text{rms}}/\hbar$, with β_r the resonator differential lever arm [32]. The resonator is also capacitively coupled to a 50 Ω waveguide (the photon feedline) on one side, and grounded on the other end, forming a hanged quarter-wave resonator (Fig. 1a) [30]. We probe the microwave response of the hybrid system recording the feedline transmission (S_{21}) at powers corresponding to less than one photon on average in the resonator (see Supplementary Note 3). By leveraging the external magnetic flux dependence of the critical current of the SQUIDs [55], the resonator frequency f_r can be tuned from ~ 6 GHz to well below 4 GHz (see Fig. 1g). To apply a finite magnetic flux, we place a superconducting coil on top of the device which generates an out-of-plane magnetic field of $50 \sim 70$ μT (see Supplementary Note 1).

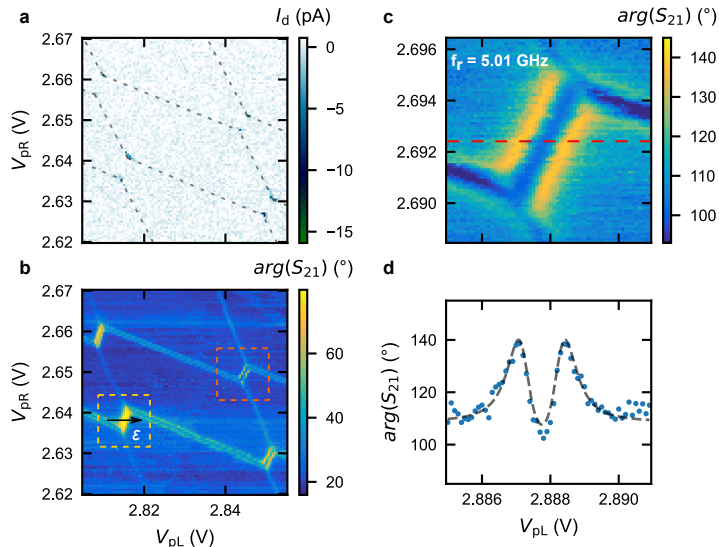


Fig. 2 DQD characterization with the tunable resonator. A region of the DQD charge stability diagram as a function of the applied plunger gate voltages V_{pR} and V_{pL} , recorded by dc-transport (a) and by measuring the phase (b) of the feedline transmission S_{21} , $\arg(S_{21})$, at $f_d = f_r = 5.01$ GHz. The resonator detects inter-dot and reservoir-dot transitions when their tunneling rates are close to f_r [56]. Yellow (orange) dashed box in b: The phase signal increases (decreases) near the inter-dot region with respect to the background, if the resonator is dispersively shifted to lower (higher) frequency. Notably, because the resonator gate lever arm is larger for the right QD, the resonator is more sensitive to its QD-reservoir transitions with respect to those of the left QD. c, Inter-dot transition probed with $f_r = 5.01$ GHz $\sim 2t_c/h$. d, A line-cut taken along the red dashed line in c. The black dashed curve shows the fit to a master equation (see Methods).

Fig. 2a shows a region of the DQD stability diagram spanned by V_{pR} and V_{pL} , measured by probing the dc current through the DQD [57]. To characterize the charge-photon coupling, we simultaneously monitor the feedline transmission at the frequency $f_d = f_r = 5.01$ GHz (see Fig. 2b). While the dc transport measurement for the explored configuration only exhibits the DQD triple points [57], the resonator response reveals not only the inter-dot transitions, but also the QD-reservoir ones, facilitating an extensive characterization of QD devices. Supplementary Figure 3 reports a zoom-out of the charge stability diagram shown in Fig. 2a and b.

Close to an inter-dot transition, the DQD system can be approximated by a simplified 2×2 charge qubit Hamiltonian, given by $H_{\text{cq}} = \frac{\varepsilon}{2}\sigma_z + t_c\sigma_x$ with corresponding eigenenergies $E_{\pm} = \pm\frac{1}{2}\sqrt{\varepsilon^2 + 4t_c^2}$. Here, σ_i represents the Pauli operator ($i = x, y, z$) [30] and ε (t_c) is the DQD energy detuning (tunnel coupling). The transverse charge-photon interaction $H_{\text{int}} = \hbar g_{\text{eff}}(a^\dagger\sigma^- + a\sigma^+)$, with $g_{\text{eff}} = 2g_0 t_c / (E_+ - E_-)$ denoting the effective charge-photon coupling strength, hybridizes the qubit with the resonator (see Supplementary Note 4). As a result, the phase of the feedline transmission S_{21} (Fig. 2b) exhibits a different response depending on whether the qubit energy is higher (yellow dashed box) or lower (orange dashed box) than the bare resonator energy.

While tuning the qubit frequency, $f_q = (E_+ - E_-)/\hbar = \sqrt{\varepsilon^2 + 4t_c^2}/\hbar$, to be close to f_r ($|f_q - f_r| < 10g_0/2\pi$) is essential to ensure a significant dispersive resonator response, it can be challenging to achieve depending on the DQD gate layout [32]. The tunable resonator presented here offers an additional means to efficiently investigate qubits by varying f_r across f_q . In Fig. 2c, we record the phase of the feedline transmission, $\arg(S_{21})$, taken with a resonator frequency of $f_r = 5.01$ GHz $\sim 2t_c/h$ to reconstruct the DQD stability diagram of an inter-dot transition. The corresponding line-cut along the red dashed line is reported in Fig. 2d. Leveraging the frequency

tunability of our resonator, we also measure the same region of the DQD stability diagram with f_r tuned above and below $2t_c/h$, reported in Supplementary Figure 4. Line-cuts across the inter-dot transition (Fig. 2d and Supplementary Figures 4g - i) are simultaneously fitted to a master equation model (denoted by black dashed lines), extracting a common tunnel coupling of $t_c/h = 2.472$ GHz, qubit decoherence $\Gamma/2\pi = 120$ MHz, and charge-photon coupling strength $g_0/2\pi = 192$ MHz for $f_r = 5.01$ GHz $\sim 2t_c/h$ (see Methods). To quantify the quality of the DQD-resonator interface, we evaluate the ratio between the coupling and the decoherence rates, by computing the cooperativity $C = 4g_0^2/(\kappa\Gamma)$ [58]. Using $\kappa/2\pi = 30$ MHz, extracted from a bare resonator fit at 5 GHz, along with the aforementioned parameters, we estimate $C \sim 40 \gg 1$, indicating the possibility to observe strong coupling.

Strong hole charge-photon coupling

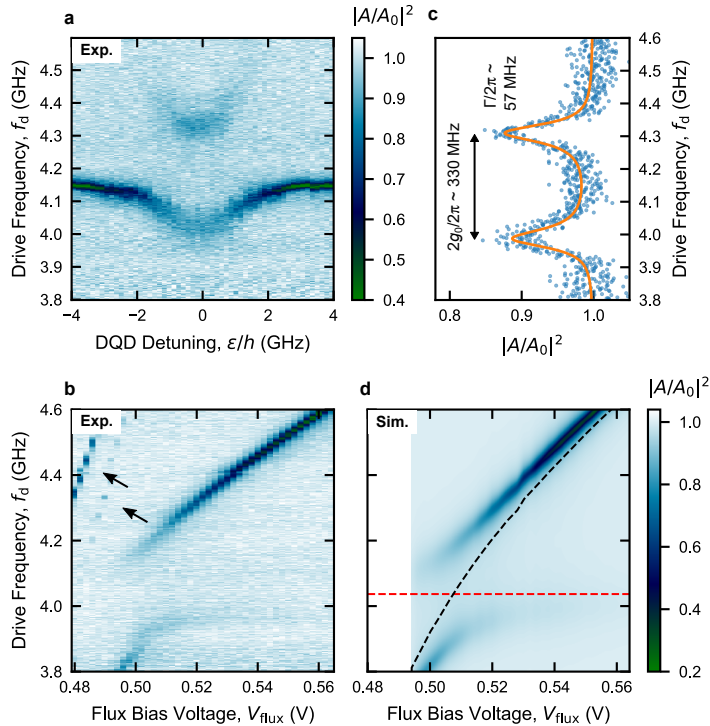


Fig. 3 Strong charge-photon coupling at the charge sweet spot. **a**, Normalized amplitude of feedline transmission $|A/A_0|^2$ as a function of drive frequency f_d and DQD detuning ϵ . An avoided crossing - the signature of the strong coupling regime - is observed when the DQD-charge transition matches the bare resonator frequency. **b**, $|A/A_0|^2$ as a function of drive frequency f_d and the voltage V_{flux} applied to the resonator coil, which tunes the resonator frequency f_r . During the measurement, the DQD is kept at $\epsilon = 0$. An avoided crossing is observed around $V_{\text{flux}} = 504$ mV, when the bare resonator frequency f_r matches the DQD charge transition ($f_r = f_q = 2t_c/h$). Higher resonator modes are visible near the half-flux point (black arrows) [53]. **c**, $|A/A_0|^2$ as a function of f_d at the resonance condition, highlighting the vacuum-Rabi splitting $2g_0/2\pi$. A fit to the master equation model is represented by a solid orange line (see Methods). All the extracted values are reported in Supplementary Table 1. $2g_0$ and Γ are indicated ($2t_c/h = 4.149$ GHz). **d**, Simulation of $|A/A_0|^2$ using input-output theory with the parameters $g_0/2\pi = 154$ MHz, $\Gamma/2\pi = 80$ MHz, $t_c/h = 2.018$ GHz extracted from fitting a line-cut of panel **b** at $V_{\text{flux}} = 504$ mV (reported in Supplementary Figure 8b).

We now probe the charge-photon interaction at $\epsilon = 0$ (charge sweet spot), where the electric dipole moment of the holes in the DQD is maximal, resulting in a vacuum-Rabi mode splitting of $2g_{\text{eff}} = 2g_0$ [26, 30]. Fig. 3a shows the normalized feedline transmission amplitude $|A/A_0|^2$ as a function of f_d and with ϵ changed to cross an inter-dot transition (as depicted by the black arrow in Fig. 2b). We note that, as we detail in Fig. 4 below, the two subsystems are not perfectly in resonance at $\epsilon = 0$ in Fig. 3a. Our resonator's frequency tunability offers a convenient way to investigate vacuum-Rabi splitting while keeping the DQD electrostatic configuration constant. This allows us to reach the resonant condition between the DQD two-level system and the resonator, while keeping the DQD gate voltages unchanged. Thereby, we fix the detuning at $\epsilon = 0$ and vary the external magnetic flux to fine-tune the resonator frequency f_r into resonance with the qubit frequency $f_q = 2t_c/h$. In Fig. 3b, we report $|A/A_0|^2$ as a function of f_d and flux bias voltage V_{flux} , where the charge-photon hybridization at ~ 4 GHz results in a clear vacuum-Rabi mode splitting. By fitting a line-cut of Fig. 3b taken at $V_{\text{flux}} = 504$ mV (reported in Supplementary Figure 8b), we extract the parameters $(t_c/h, g_0/2\pi, \Gamma/2\pi) = (2018, 154, 80)$ MHz. These parameters are utilized to numerically reconstruct $|A/A_0|^2$ (Fig. 3d). To better evaluate the cooperativity of our

system, in Fig. 3c we report a high-quality vacuum-Rabi mode splitting measured, with increased averaging, as a function of f_d in the same DQD configuration ($\varepsilon = 0$), but at $V_{\text{flux}} = 507$ mV to compensate for a slight drift in qubit frequency. By fitting to the master equation model (solid line in Fig. 3c, see Methods), we find $(t_c/h, g_0/2\pi, \Gamma/2\pi) = (2072, 165, 57)$ MHz. These parameters result in a cooperativity of $C \sim 100$ (with $\kappa/2\pi = 19$ MHz), which highlights the strong charge-photon coupling in planar Ge.

In Supplementary Figure 9a, we explore an alternative DQD charge transition, which features an enhanced g_0 . Fitting the line-cut in Supplementary Figure 9b to the master equation model, we extract the parameters $(t_c/h, g_0/2\pi, \Gamma/2\pi) = (2711, 260, 192)$ MHz, and calculate a cooperativity of $C \sim 23$ (with $\kappa/2\pi = 63$ MHz). Here, the high $g_0/2\pi = 260$ MHz, enabled by the high-impedance SQUID array resonator, allows us to achieve the strong coupling regime, in spite of a substantial qubit decoherence rate Γ . We speculate that the difference between the values of g_0 and Γ extracted from the two datasets in Fig. 3 and Supplementary Figure 9 may arise from distinct effective electric dipole moments associated with the two DQD electrostatic configurations [29]. To account for the frequency dependence of the coupling strength between the resonator and DQD, we calculate the resonator's differential lever arm $\beta_r = \frac{2g_0\hbar}{V_{0,\text{rms}}}$ in the two configurations. We find β_r values of 0.18 and 0.25 eV/V (see Methods), respectively, indicating a higher coupling of the resonator to the detuning degree of freedom in the second case, albeit at the cost of a larger Γ [29].

Tunable high-impedance resonator for qubit spectroscopy

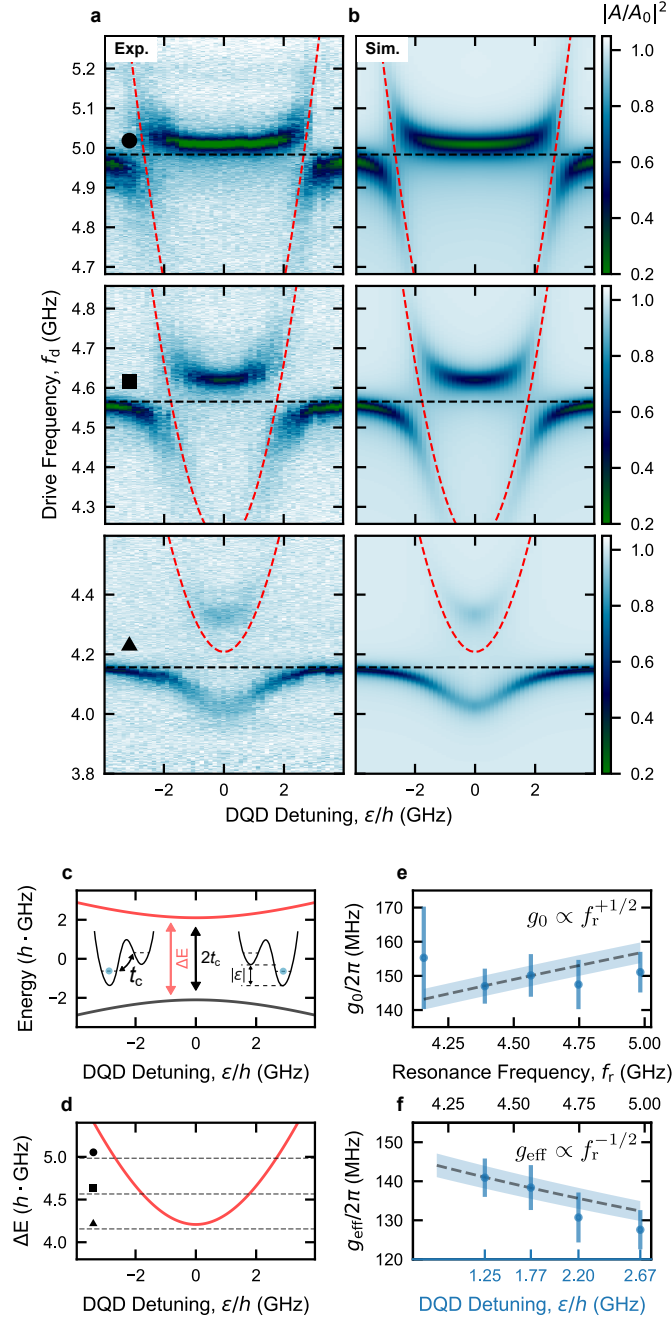


Fig. 4 Charge qubit spectroscopy via tunable resonator. **a**, Normalized amplitude of feedline transmission $|A/A_0|^2$ as a function of drive frequency f_d and DQD detuning ϵ . The three panels are taken in correspondence of three different bare resonator frequencies f_r , denoted by black circle, square and triangle, while keeping the inter-dot tunnel coupling t_c constant. **b**, Simulation of $|A/A_0|^2$ using input-output theory with the parameters extracted by fitting the full dataset in the corresponding panels in **a** to the master equation model (see Methods). Black (red) dashed lines in **a** and **b** denote the bare resonator (DQD-charge qubit) frequency. **c**, Energy-level diagram, i.e. the energy spectrum, of the DQD charge qubit system as a function of DQD detuning ϵ (calculated for the charge qubit Hamiltonian in main text). The black (red) curve represents the ground (excited) state of the charge qubit. Inset: DQD potential schematics showing the charge state at the negative and positive ϵ . **d**, Excitation energy ΔE as a function of DQD detuning ϵ . The dashed lines denoted by black circle, square and triangle correspond to different f_r in **a**. **e**, Extracted charge-photon coupling strength g_0 as a function of f_r . **f**, Effective charge-photon coupling strength g_{eff} at the ϵ values for which the two subsystems are in resonance, estimated using $g_{\text{eff}} = g_0 2t_c / h f_r$. The DQD detuning values corresponding to the avoided crossings are indicated at the bottom axis in blue. Since the resonance condition is not met for the lowest panel in **a** ($f_r < 2t_c/h$), the first point in **f** is omitted. The dashed lines in **e** and **f** represent the expected trend of the coupling strengths as a function of f_r , while the error bars and the shaded regions indicate the estimated uncertainties (see Methods).

We leverage the resonator frequency tunability to conduct resonant energy spectroscopy of the DQD charge qubit, in the same DQD configuration as in Fig. 3, and keeping the DQD at a fixed t_c [30]. This spectroscopy

aims to reconstruct the qubit's energy dispersion. In contrast to the measurements in Fig. 3, where $f_r \sim 2t_c/h$, here we extend our investigation also to higher resonator frequencies, $f_r > 2t_c/h$.

In Fig. 4a, we present the measured normalized feedline transmission $|A/A_0|^2$ as a function of f_d and ε for three different values of f_r , as indicated by dashed lines in Fig. 4d. The schematics in Figs. 4c and d illustrate the charge qubit energy level diagram (panel c) and the excitation energy spectrum $\Delta E = E_+ - E_- = E_{cq}$ (panel d) along ε . Notably, clear avoided crossings are observed in Fig. 4a when the charge qubit gets in resonance with the resonator ($hf_r = \sqrt{\varepsilon^2 + 4t_c^2}$). Additional details on the charge qubit spectroscopy are available in Supplementary Note 5.

These spectroscopy measurements also provide valuable insights into the evolution of the effective charge-photon coupling strength g_{eff} , as a function of the DQD detuning ε . By fitting all five datasets presented in Supplementary Figure 10a to the master equation model, we accurately reproduce the hybridized charge qubit-resonator spectra, as shown in Fig. 4b and Supplementary Figure 10b. For this fit, the full 2D datasets are considered and a detuning dependence of the qubit decoherence rate $\Gamma(\varepsilon)$ is included in the model (see Methods for more details).

From these spectra, we extract the charge-photon coupling strengths g_0 , and present them as a function of f_r in Fig. 4e. We also estimate the effective charge-photon coupling strengths $g_{\text{eff}} = g_0 2t_c / \sqrt{\varepsilon^2 + 4t_c^2} = g_0 2t_c / hf_r$, when the two systems are in resonance, and report them as a function of both ε and f_r in Fig. 4f. Since $g_0 = \frac{1}{2}\beta_r V_{0,\text{rms}}/\hbar = \frac{1}{2}\beta_r 2\pi f_r \sqrt{Z_r/(2\hbar)}$, where the lumped equivalent resonator impedance Z_r can be written in terms of f_r as $Z_r = 1/(2\pi f_r C_r)$, we obtain a frequency dependence of $g_0 \propto \sqrt{f_r}$ and hence $g_{\text{eff}} \propto 1/\sqrt{f_r}$ (assuming constant C_r and resonance condition). The dashed line in Fig. 4e represents a fit of the extracted g_0 to the expected frequency dependence. Using this fit, we estimate the evolution of g_{eff} as a function of f_r and illustrate it as a dashed line in Fig. 4f. Notably, the evolution of g_0 does not closely follow the expected trend as a function of f_r . This discrepancy can be attributed to a nonuniform and frequency-dependent voltage profile of the resonator mode, potentially due to magnetic flux inhomogeneity along the SQUID array. Alternatively, simultaneous hybridization of the DQD with higher order resonator modes (see Fig. 1g), which approach the qubit frequency in the studied flux range, may influence the coupling to the fundamental mode. Further investigation is required in order to better understand the evolution of g_0 .

Hybrid circuit QED with strongly correlated states

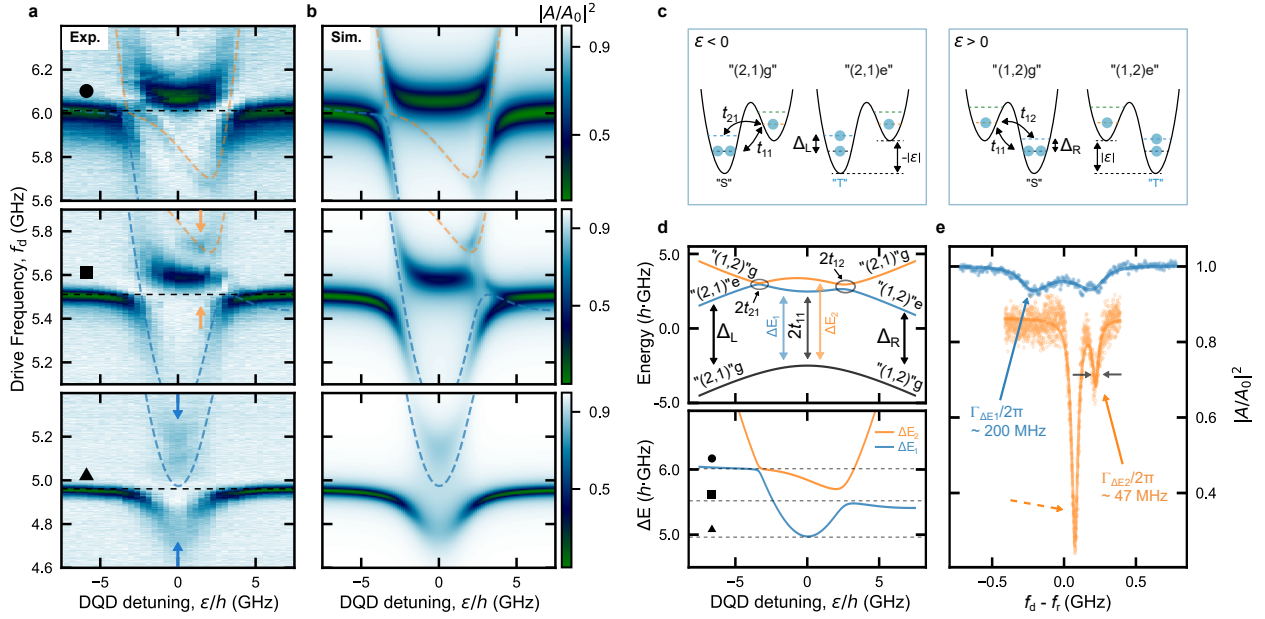


Fig. 5 Spectroscopy of the strongly correlated states in the hybrid architecture. **a**, Normalized amplitude of feedline transmission $|A/A_0|^2$ as a function of drive frequency f_d and DQD detuning ε . The three panels are taken in correspondence of three different bare resonator frequencies f_r (black dashed lines denoted by black circle, square and triangle). The dashed blue and orange lines show the calculated excitation spectra of the DQD, as detailed in panel **d**, revealing the presence of quenched strongly correlated states (SCSs). **b**, Simulation $|A/A_0|^2$ using a generalized input-output theory of a multi-level DQD system (see Methods, and Supplementary Note 7) and for the three different f_r as in **a**. The parameters for the simulations can be found in Supplementary Table 3. **c**, DQD schematics of the states relevant to “(2,1)” and “(1,2)” charge configurations for negative and positive DQD detuning ε . Δ_L (Δ_R) is the singlet-triplet energy splitting Δ_{ST} when two holes are paired in the left (right) QD. **d**, Energy-level diagram (top panel) and excitation energy ΔE (bottom panel) calculated with the 4×4 Hamiltonian in Methods, and used for the input-output simulation in **b**. In the bottom panel, the blue (orange) curve corresponds to the energy splitting ΔE_1 (ΔE_2) between the first (second) excited state branch and the ground state, shown in the top panel. The black dashed lines denoted by a black circle, square, and triangle in the bottom panel represent the different f_r used for acquiring the distinct spectra in **a**. **e**, Frequency line-cut taken at the DQD detuning indicated by the blue (orange) arrows in **a**. The blue (orange) data highlights the resonator hybridization with the ΔE_1 (ΔE_2) transition. A fit to the master equation model (solid blue line), and Lorentzian (solid orange line) results in $\Gamma_{\Delta E_1}/2\pi \sim 200$ MHz and $\Gamma_{\Delta E_2}/2\pi \sim 47$ MHz, respectively. The orange dashed arrow indicates the resonator dispersively shifted by the interaction with the charge-like excitation ΔE_1 .

Strikingly, our investigation of multiple adjacent inter-dot transitions reveals that the conventional charge qubit-like spectroscopy, as illustrated in Fig. 4, featuring a single two-level system coupled to the resonator, fails to describe several cases. For instance, in Fig. 5a, we present three independent measurements of the normalized feedline transmission $|A/A_0|^2$ as a function of f_d and ε , obtained for the same DQD configuration, but in correspondence to three different resonance frequencies f_r (indicated by black dashed lines denoted by a black circle, square, and triangle). See Supplementary Figure 12 for a more detailed resonator spectroscopy. These measurements unveil unconventional features, including anomalous spectroscopy diagrams asymmetric in ε , additional avoided crossings, and distinct spectroscopic lines that deviate significantly from the conventional model for a resonator hybridized with a two-level system and have not been previously documented.

The anomalous spectrum of these DQD configurations is captured by an extended model that includes an excited state in each QD, whose energies can be close to hf_r . Specifically, we adopt a 4×4 Hamiltonian similar to the one used in prior studies [52, 59] and numerically simulate the DQD spectrum and feedline transmission. We assume the validity of an effective hole numbering, where we neglect the even core holes (see Methods). More specifically, in modelling Fig. 5a, we assume a “(2,1)” \leftrightarrow “(1,2)” DQD charge configuration (odd case). Within the “(2,1)” configuration, the two holes in the left QD can occupy either the ground orbital state, forming “(2,1)g”, or the excited orbital state, forming “(2,1)e” (see Fig. 5c, for $\varepsilon < 0$). Analogously, for $\varepsilon > 0$, the eigenstates consist of the ground and excited states of the right QD, corresponding to “(1,2)g” and “(1,2)e”, respectively (see Fig. 5c, for $\varepsilon > 0$).

As we demonstrate in detail below, making use of Fig. 6, such an effective particle numbering in the QDs readily captures spin structures that depend on the hole number parity [32, 54, 60]. In this regard, we expect distinct spin symmetries in our “(2,1)” \leftrightarrow “(1,2)” configuration related to the ground and excited states [52]. More explicitly, we assume the ground (excited) state to involve anti-symmetric singlet “S” (symmetric

triplet “T”) spin pairing in the doubly-occupied QD (Fig. 5c). In this configuration, the two lowest energy levels form doublet spin states together with the single spin in the other QD [52]. For instance, “(2, 1)g” (“(2, 1)e”) forms a doublet state with spin singlet (triplet) pairing in the left QD. Here, finite exchange interaction can couple the ground and excited doublet states [52, 59], because they have the same total spin quantum number $S_{\text{tot}} = 1/2$, despite the different spin symmetries within the doubly-occupied QD. With this exchange interaction, the “(2, 1)g” \leftrightarrow “(2, 1)e” or “(1, 2)g” \leftrightarrow “(1, 2)e” transitions can be revealed by our resonator as presented in Fig. 5a, in agreement with the spin selection rule.

Based on the above modeling, we empirically determine the Hamiltonian parameters, including $\Delta_L/h = 5.40$ GHz ($\Delta_R/h = 4.73$ GHz), i.e. the singlet-triplet splitting Δ_{ST} in the left (right) QD, that accurately reproduce both the energy and excitation spectra, reported respectively in the top and bottom panels of Fig. 5d (see Supplementary Table 4). We also estimate the tunnel coupling strengths between the i^{th} state of the left QD and the j^{th} state of the right QD, t_{ij} . Furthermore, we use input-output theory to analyze the interaction between the resonator and the multi-level QD system [61] (see Methods and Supplementary Note 7), enabling us to accurately reproduce the spectrum of the hybridized system, as depicted in Fig. 5b. Note that for this, it is essential to assume finite tunnel coupling strengths $t_{12}/h = 0.21$ GHz and $t_{21}/h = 0.11$ GHz.

The extracted values of $\Delta_{L,R}$ are orders of magnitude smaller than the expected orbital energy gap (~ 70 h·GHz) obtained from a single particle model, considering the dimensions of our QDs (see Supplementary Note 6). Instead, these estimated excitation energies are generated by strong Coulomb correlation effects within each QD. To support this interpretation, in Supplementary Note 6, we present a preliminary model for two interacting holes in planar Ge, which suggests that the small anisotropy in the QD confinement, in conjunction with electron-electron interactions, can result in strongly correlated states (SCSs) with $\Delta_{\text{ST}} \lesssim 10$ h·GHz. Although a more comprehensive investigation based on full-configuration-interaction calculations is necessary to precisely characterize the energy scales within the DQD [42, 47], our preliminary analysis provides evidences that the observed features in Fig. 5a may be attributed to WM states [38, 45–50].

As described above, we note that SCSs exhibit distinct spin symmetries, with the ground orbital state supporting the anti-symmetric spin singlet, and the excited orbital state supporting the symmetric spin triplet [40, 52] (see Fig. 5c). These symmetries imply that the relaxation between the states specified above involves a spin-changing process, which can be considerably slower compared to the bare charge relaxation [40, 52]. We explore this distinction in Fig. 5e, which presents two line-cuts along ε , marked by the orange and blue dashed lines in the middle and bottom panels of Fig. 5a. In comparison to the charge qubit-like decoherence rate $\Gamma_{\Delta E_1}/2\pi \sim 200$ MHz extracted from the fit to the master equation (blue solid line in Fig. 5e), the second excited state spectrum ΔE_2 (denoted by an orange solid arrow in Fig. 5e) is characterized by a significantly narrower linewidth $\Gamma_{\Delta E_2}/2\pi \sim 47$ MHz (extracted from the fit to the Lorentzian), which is further supporting our modeling. Similar spectroscopic signatures, attributed to the SCSs with excitation energies very close to that of the resonator, have been detected across multiple inter-dot transitions. Supplementary Figure 13 reports another instance of a similar spectrum exhibiting $\Gamma_{\Delta E_2}/2\pi \sim 35$ MHz.

The presented Hamiltonian also models a spin-charge hybrid qubit, which can be encoded in the SCSs exhibiting a lower decoherence rate in comparison to a bare charge qubit. Such a hybrid qubit also allows all-electrical control of the spin states based on exchange interaction [41, 52].

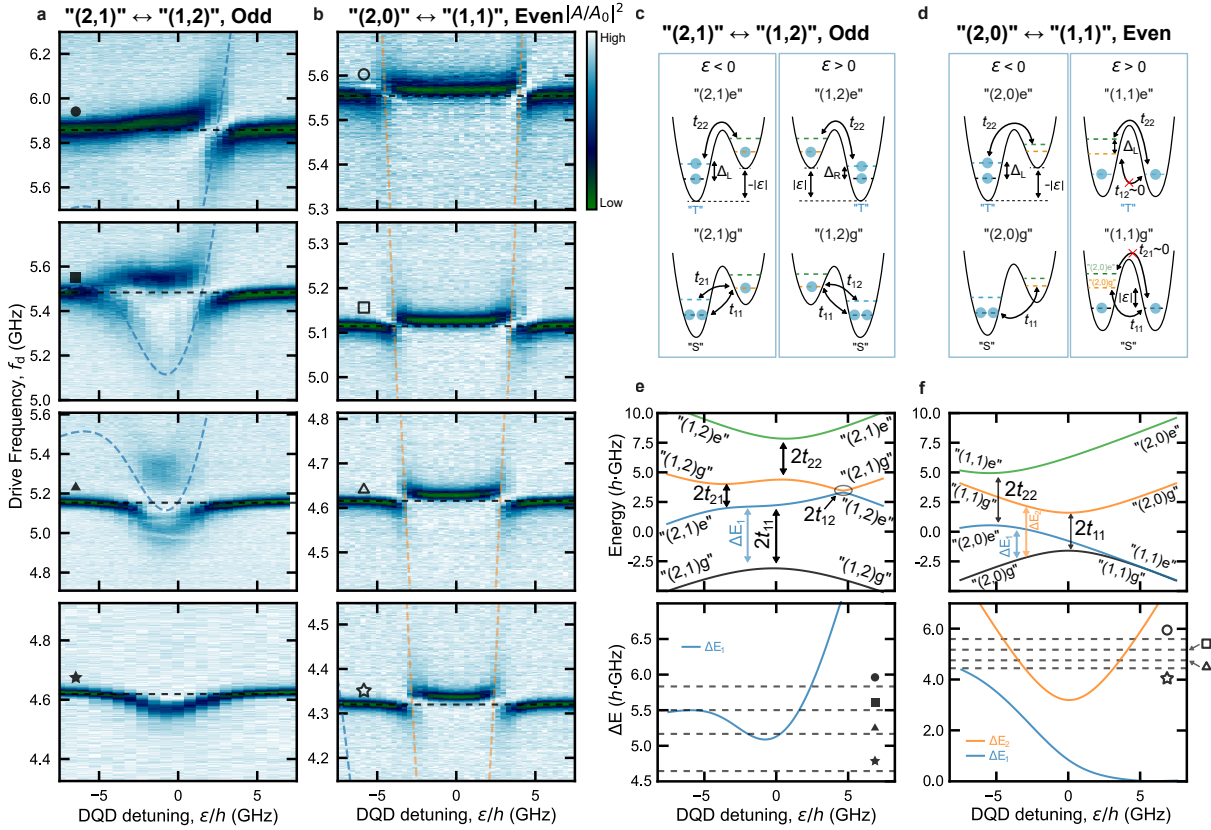


Fig. 6 Hole number parity-dependent behavior. **a, b,** DQD resonant spectra measured for two adjacent inter-dot transitions $"(2,1) \leftrightarrow (1,2)"$ (odd, **a**) and $"(2,0) \leftrightarrow (1,1)"$ (even, **b**). Each panel presents the normalized amplitude of feedline transmission $|A/A_0|^2$ as a function of drive frequency f_d and DQD detuning ε , obtained in correspondence of the bare resonator frequency indicated by the horizontal black dashed line. The dashed blue and orange lines show the calculated first, and second excitation spectra of the DQD, as detailed in panel **e** and **f**, revealing the presence of quenched SCSs. **c, d,** Schematics of the relevant states for $"(2,1) \leftrightarrow (1,2)"$ (**c**, identical to the one shown in Fig. 5c) and $"(2,0) \leftrightarrow (1,1)"$ (**d**) inter-dot transition. In the even parity case **d**, the energy gap between $"(1,1)g"$ and $"(1,1)e"$, $\Delta_R \sim 0$ due to the negligible exchange interaction of the unpaired holes. Δ_L is fixed to the value used in the odd case because the number of the holes in the left QD is unchanged. In the $"(1,1)"$ charge state, "S" ("T") denotes the spin singlet (triplet) state formed by the two holes in the respective QD. $t_{12}, t_{21} \sim 0$ due to the spin selection rule. **e, f,** Energy level diagram (top panel) and excitation energy ΔE (bottom panel) calculated with the 4×4 Hamiltonian described in Methods, to obtain the resonant spectra in **a** and **b**, respectively. In the bottom panel, the blue (orange) curve corresponds to the energy splitting ΔE_1 (ΔE_2) between the first (second) excited state branch and the ground state, shown in the top panel. The black dashed lines denoted by the different black filled (blank) symbols in the bottom panel of **e** (**f**) represent the different f_r used for acquiring the distinct spectra in **a** (**b**).

To further explore these unconventional DQD spectra due to strong Coulomb correlation effects, and to confirm the intrinsic spin nature of the aforementioned states, we delve into the expected hole number parity-dependence, distinguishing between even and odd effective DQD occupation. As we detail below, the observed energy spectra measured with our resonator both in the even and odd configurations are consistent with the spectra derived from our effective model, which takes into account the parity dependent spin structures. In Figs. 6a and b, we investigate a representative instance of two neighboring inter-dot transitions involving effective charge configurations $"(2,1) \leftrightarrow (1,2)"$ and $"(2,0) \leftrightarrow (1,1)"$, respectively (denoted in the stability diagram in Supplementary Figure 14a by the dashed black and red boxes).

In the $"(2,1) \leftrightarrow (1,2)"$ configuration (Fig. 6a), characterized by an odd total number of holes, the ground and first excited states have the same spin quantum number $S_{\text{tot}} = 1/2$. Similar to the configuration shown in Fig. 5, this results in a finite exchange interaction between $"(2,1)g"$ and $"(2,1)e"$, and between $"(1,2)g"$ and $"(1,2)e"$, enabling their electrical coupling to the resonator, in accordance with the spin selection rule. To faithfully replicate both energy and excitation spectra shown in Fig. 6e, it is essential to assume a sizable t_{21} and a relatively small $\Delta_L/h \sim 5.48$ GHz. In contrast to Fig. 5a, the resonator spectroscopy reported in Fig. 6a does not show the second excitation ΔE_2 , due to the larger Δ_R with respect to f_r .

For the adjacent even configuration, denoted as $"(2,0) \leftrightarrow (1,1)"$ (see Figs. 6b and d), with a single additional hole in the right QD compared to the odd configuration, the total spin numbers of the ground ($S_{\text{tot}} = 0$) and first excited states ($S_{\text{tot}} = 1$) in the DQD are different. This is further supported by the observed signatures of Pauli spin blockade (PSB) presented in Supplementary Note 9. Because the number of holes in the left QD is the same as in the configuration presented in Fig. 6a, we expect a similar Δ_L between the

“(2,0)g” and “(2,0)e” states. The extracted width of the PSB window $w_{\text{PSB}}/h \sim 7.8 \pm 1.2$ GHz is comparable to $\Delta_{\text{L}}/h \sim 5.48$ GHz used for the simulation of the energy diagram in the odd configuration in Fig. 6e. In our system with a magnetic field $B \ll 1$ mT, the effect of the spin-orbit interaction or Zeeman splitting difference between the two QDs can be neglected [10, 54]. Consequently, $t_{12}, t_{21} \sim 0$ in the model Hamiltonian, and the resonator electric field can only drive spin-preserving transitions. Furthermore, in the “(1, 1)” configuration, the spatial separation of the two holes results in a negligible exchange splitting between the “(1,1)g” and “(1,1)e” states (Fig. 6d), allowing us to set $\Delta_{\text{R}} \sim 0$ in the model Hamiltonian. This leads to the energy diagram depicted in Fig. 6f, which explains the observation of a conventional charge-qubit-like spectrum reported in Fig. 6b, corresponding to the charge transition “(2, 0)g” \leftrightarrow “(1, 1)g” with excitation energy ΔE_2 . We also demonstrate that the master equation model constructed using our extended effective Hamiltonians closely reproduces the measured spectra of the hybridized multi-level DQD-resonator system (Figs. 6a and b) for both odd and even configurations, as reported in Supplementary Note 10.

As a side note, we observe faint additional features in some of our 2D spectroscopy datasets, such as the ones around 5 GHz in Fig. 6a. These features may be attributed to uncontrolled two-level fluctuators in the tunneling junctions of the SQUID array resonator, which can capacitively couple to the microwave photons (see Supplementary Note 3) [62]. Alternatively, transitions between higher DQD energy levels, which are observable due to a finite thermal population of the excited state, might also explain some of these extra avoided crossings. However, accurately modeling these transitions would require the introduction of additional energy states into our model, which is beyond the scope of this work.

3 Discussion

In this study, we have demonstrated the potential of a hybrid architecture, combining a superconductor cavity with semiconductor QDs for advancing hole-based quantum information processing in planar germanium. Leveraging a high-impedance Josephson junction-based resonator with tunable frequency, we have demonstrated strong hole charge-photon coupling. This achievement is substantiated by our observation of charge-photon vacuum-Rabi mode splitting and the high cooperativity value ($C \sim 100$) estimated for our hybrid system. Furthermore, the frequency tunability of our resonator has enabled us to successfully resolve strongly correlated states (SCSs) within QDs in planar Ge structures. The distinct spin symmetries of the SCSs lead to significantly reduced decoherence rates of the higher excited levels, a promising development for establishing strong spin-photon coupling. The interaction between QD SCSs and a frequency-tunable resonator provides a very effective avenue for exploring complex many-body electronic states in multi-level QDs. While a detailed measurement of the charge density distribution of the ground state is required to unambiguously prove the Wigner molecularization process [44], the presence of strong Coulomb correlation and QD confinement anisotropy, as suggested by our simulations, make Wigner molecules the most plausible model to describe the observed quenching of strongly correlated states in our QDs [38, 45–50]. Our findings facilitate coherent photon coupling with spin-charge hybrid qubits, also potentially based on longitudinal interaction through singlet-triplet splitting modulation [63]. In conclusion, we have demonstrated the ability to coherently exchange a photon with holes in planar Ge, marking a critical step toward achieving long-distance spin-spin entanglement. Our work lays the foundation for future research on hole-photon coupling and long-range interactions of hole-based qubits, paving the way for the development of large-scale quantum processors.

4 Methods

Device fabrication

The hybrid triple QD device is fabricated on a Ge/SiGe heterostructure grown by low-energy plasma-enhanced chemical vapor deposition (LEPECVD) using a forward grading technique (see Fig. 1b) [54]. The device fabrication is entirely carried out at the Center of MicroNano Technology (CMi) at EPFL. As a first step, 60 nm Pt markers and ohmic contacts are patterned by E-beam lithography (EBL), evaporation and lift-off. Immediately before the deposition, a 20 s dip in diluted HF (1%) removes the native oxide in the opened regions to ensure a low-resistive ohmic contact. The two-dimensional hole gas (2DHG) is self-accumulated in the 16 nm Ge quantum well (QW). Therefore, a 110 s reactive ion etching (RIE) step etches ≈ 80 -90 nm, leaving a well defined conductive channel from one ohmic contact to the other. The reacting plasma is based on SF₆, CHF₃ and O₂ and the mask is patterned by EBL. A 15 s dip in buffered HF (BHF) etches away the native oxide immediately before the gate oxide deposition, a 20 nm atomic layer deposition (ALD) Al₂O₃. The deposition temperature is 300°C. Then, a 15 min rapid thermal annealing (RTA) in forming gas (N₂/H₂ 5%) at 300°C ensures that the Pt properly diffuses down to the Ge QW. The single-layer gates are patterned in two steps by EBL, evaporation and lift-off. This ensures that the thin 3/22 nm Ti/Pd gates are patched on the etched step by 3/97 nm ones, routed out to the bonding pads. The superconducting part of the device is again patterned in two steps by EBL, evaporation and lift-off. First, the waveguide and the ground plane (120 nm of Al) and, lastly, the SQUID array resonator, following the conventional Dolan-bridge double angle evaporation method for Josephson junctions (JJs). The bottom Al layer is 35 nm thick, whereas the top one is 130 nm. The tunneling oxide barrier is grown by filling the chamber with O₂ at a pressure of 2 Torr for 20 min (static oxidation) without breaking the vacuum. From measurements of the SQUID array resistance at room temperature, we estimate a critical current of about 522 nA per SQUID.

Fitting procedure for a conventional cavity-dressed charge qubit

The experimental data shown in this work reporting the feedline transmission S_{21} are fitted to a master equation model (see Supplementary Note 4 for the full derivation) and normalized by a background trace to remove the standing wave pattern present in the feedline transmission. The background reference trace is obtained by tuning the resonance frequency of the resonator outside the frequency region of interest by making use of the superconducting coil and recording a high-power trace. The complex transmission of a resonator hanged to a 50 Ω feedline and coupled to a charge qubit reads as:

$$S_{21} = ae^{i\alpha} e^{-2\pi if_d \tau} \frac{\Delta_r - i(\kappa - |\kappa_{\text{ext}}|e^{i\phi})/2 + g_{\text{eff}}\chi}{\Delta_r - i\kappa/2 + g_{\text{eff}}\chi}, \quad (1)$$

where $\Delta_r = \omega_r - \omega_d$ is the resonator-drive detuning, $\kappa = \kappa_{\text{ext}} + \kappa_{\text{int}}$ the total resonator linewidth given by both coupling to the waveguide $\kappa_{\text{ext}} = |\kappa_{\text{ext}}|e^{i\phi}$ and internal losses κ_{int} , $g_{\text{eff}} = g_0 \frac{2t_c}{\sqrt{\varepsilon^2 + 4t_c^2}}$ the effective charge-photon coupling strength, ε the DQD detuning, t_c the inter-dot tunneling coupling, $\chi = \frac{g_{\text{eff}}}{-\Delta_q + i\Gamma}$ the DQD susceptibility, $\Delta_q = \omega_q - \omega_d$ the qubit-drive detuning, with the qubit frequency $\omega_q/2\pi = \sqrt{\varepsilon^2 + 4t_c^2}/h$, and Γ the charge qubit linewidth. a , α , τ , and ϕ are correction factors that take into account the non-ideal response of the cavity due to the environment. Further information is provided in Supplementary Note 4. The resonator parameters f_r , κ and κ_{ext} , as well as the environmental factors, are obtained by separately fitting S_{21} for the bare uncoupled resonator.

The simultaneous fit of the line-cuts reported in Fig. 2d and Supplementary Figures 4g - i is performed using common fitting parameters for t_c and Γ , while using separate g_0^k , where $k = g, h, i$ for the three different datasets. In order to convert the voltage axis to DQD detuning $\varepsilon = \mu_L - \mu_R = \beta_{\text{pL}}V_{\text{pL}} - \beta_{\text{pR}}V_{\text{pR}}$, the differential lever arms $\beta_{\text{pL}} = \alpha_{\text{pL}}^L - \alpha_{\text{pL}}^R = 0.031$ and $\beta_{\text{pR}} = \alpha_{\text{pR}}^R - \alpha_{\text{pR}}^L = 0.016$ are extracted from Coulomb diamond and DQD charge stability diagram measurements. Here, μ_L (μ_R) is the electrochemical potential of the left (right) QD, α_{pL}^L (α_{pR}^R) is the lever arm for the left (right) plunger gate and α_{pL}^R (α_{pR}^L) is the cross-lever arm for the left (right) plunger gate.

Fig. 3c is obtained from a separate measurement with respect to Fig. 3a, with higher resolution and integration time and taken at a slightly different flux point ($V_{\text{flux}} = 507$ mV). The resonator parameters used for generating Fig. 3d are obtained from fitting the bare resonator as a function of V_{flux} , similar to the measurement in Fig. 1g (see Supplementary Figure 6). The other parameters are obtained from fitting a frequency line-cut of Fig. 3b at $V_{\text{flux}} = 504$ mV (see Supplementary Figure 8b), where the two subsystems are in resonance, to the master equation model described above. Note that here, the lowest frequency of the measurement is 3.8 GHz, limited by the bandwidth of the cryogenic circulators. To help interpret the different extracted g_0 for the datasets in Fig. 3a and Supplementary Figure 9, the resonator differential lever arm is calculated for both cases, following

the relation $g_0 = \frac{1}{2}\beta_r V_{0,\text{rms}}/\hbar = \frac{1}{2}\beta_r 2\pi f_r \sqrt{\frac{Z_r}{2\hbar}}$ [32]. Using $Z_r = 1.6 \text{ k}\Omega$ (1.2 k Ω) and $f_r = 4.149 \text{ GHz}$ (5.432 GHz) for Fig. 3a (Supplementary Figure 9a), we get $V_{0,\text{rms}} = 7.6 \text{ }\mu\text{V}$ (8.7 μV) and $\beta_r = 0.18 \text{ eV/V}$ (0.25 eV/V). For further details about the resonator equivalent lumped impedance and its frequency, see Supplementary Notes 3.

In contrast to Fig. 3, the fits presented in Fig. 4 and Supplementary Figure 10 are performed simultaneously on all the 2D spectroscopy datasets. To account for the detuning dependence of the qubit dephasing rate due to charge noise, we include a DQD detuning dependence of the qubit decoherence in the form of $\Gamma = \Gamma_0 + \Gamma_\varepsilon \frac{1}{\hbar} \frac{\partial \omega_q}{\partial \varepsilon} = \Gamma_0 + \Gamma_\varepsilon \frac{\varepsilon}{\hbar \omega_q}$ [23, 64, 65], where the derivative $\frac{\partial \omega_q}{\partial \varepsilon}$ quantifies the sensitivity of the qubit energy, and hence the scaling of the qubit dephasing rate, with respect to detuning noise induced by charge noise in the environment. For the combined fit, the DQD tunnel coupling t_c , the differential lever arm β_{pL} of the left plunger gate as well as the constant and detuning-dependent decoherence coefficients Γ_0 and Γ_ε , respectively, are shared among all five datasets, while the charge-photon coupling strength g_0 , a voltage offset V_{pL}^0 that corresponds to $\varepsilon = 0$ and all the resonator parameters are fitted independently for each dataset. Γ_0 was fixed to 57 MHz, extracted from the fit in Fig. 3c. However, we verified that this does not have any influence on the estimated values for g_0 . We extract a value of $\Gamma_\varepsilon \sim 164 \text{ MHz}$ from the fit. All resonator parameters (see Eq. (1)), except for the bare resonator frequency f_r , are estimated by fitting a single trace of S_{21} taken at large DQD detuning ε . The error bars in Figs. 4e and f correspond to the 2σ confidence interval estimated by propagating the errors of κ and κ_{ext} taken from the separate resonator fit. The dashed line in Fig. 4e represents a fit (including the errors of g_0) of the extracted g_0 values to the relation $g_0 = a \cdot \sqrt{f_r}$. The resulting evolution of g_0 is then converted to $g_{\text{eff}} = g_0 2t_c/f_r$ and reported in Fig. 4f. The shaded regions in Figs. 4e and f correspond to the 2σ confidence interval extracted from the last fit above.

Hamiltonian for SCS simulation

To numerically reproduce the hybridized DQD-resonator spectra obtained from the microwave feedline transmission shown in Figs. 5, 6, Supplementary Note 8 and Supplementary Note 10, we need, as a first step, to identify the multi-level energy spectra characterizing the DQD in each configuration.

We model the DQD assuming a 4×4 toy-model Hamiltonian identical to the spin-charge hybrid qubit defined by three-particles in a DQD [52, 59], as reported below. The Hamiltonian is written in the position basis $[|L_g\rangle, |L_e\rangle, |R_g\rangle, |R_e\rangle]$, where L (R) denotes the charge state with the excess hole in the left (right) QD. g and e present the ground and excited states of the corresponding charge configuration, respectively. Specifically, in the case of an odd total number of holes in the DQD, $L = (2n + 2, 2m + 1)$ and $R = (2n + 1, 2m + 2)$. Here, we use the notation (p, q) to denote the DQD charge number configuration with p (q) representing the number of holes in the left (right) QD. Throughout this work, the $2n$ ($2m$) core holes in the left (right) QD play no role, reducing the effective DQD charge number to $L = "(2, 1)"$ and $R = "(1, 2)"$, respectively. Similarly, in the even configuration, the relevant charge states effectively become $L = "(2, 0)"$, and $R = "(1, 1)"$. Consequently, the basis in which the Hamiltonian is expressed is $["(2, 1)g", "(2, 1)e", "(1, 2)g", "(1, 2)e"]$ in the odd configuration and $["(2, 0)g", "(2, 0)e", "(1, 1)g", "(1, 1)e"]$ in the even one (see Figs. 6c and d for the schematic visualisation of these states). In this basis, the DQD 4×4 Hamiltonian reads:

$$H = \begin{bmatrix} \varepsilon/2 & 0 & t_{11} & t_{12} \\ 0 & \eta_L \varepsilon/2 + \Delta_L & t_{21} & t_{22} \\ t_{11} & t_{21} & -\varepsilon/2 & 0 \\ t_{12} & t_{22} & 0 & -\eta_R \varepsilon/2 + \Delta_R \end{bmatrix} \quad (2)$$

Here, ε is the DQD detuning, Δ_L (Δ_R) is the singlet-triplet splitting Δ_{ST} when two holes are paired in the left (right) QD and t_{ij} denotes the tunnel coupling between the i^{th} state of left QD and j^{th} state of right QD. We also include $\eta_L = 0.92$ ($\eta_R = 0.913$) to account for the different lever arms of the excited states in Fig. 5 [47].

The Hamiltonian eigenvalues are used to reconstruct the energy spectra (eigenenergies vs ε/\hbar) reported in Figs. 5d and 6e, f (top panels), whereas the excitation spectra, i.e. the energy differences between excited states and the ground state, are displayed in the bottom respective panels.

In the odd total hole number configuration, $"(2, 1)k" \leftrightarrow "(1, 2)k"$, with $k = g, e$ (Figs. 5 and Figs. 6a), the ground and the first excited states have the same total spin number $S_{\text{tot}} = 1/2$. For example $"(2, 1)g"$ and $"(2, 1)e"$ form the doublet spin states with an energy splitting given by the exchange interaction of the paired holes in the left QD [52]. Thereby, a finite tunnel coupling between ground and exchange-split excited states is allowed, e.g. $t_{12}, t_{21} > 0$, by spin-selection rules [52]. Both the QDs can have $\Delta_{\text{ST}}/\hbar \sim 5 \text{ GHz}$ (close to resonator frequency) when a SCS is formed in each QD.

In contrast, in the even configuration, $"(2, 0)k" \leftrightarrow "(1, 1)k"$ (Fig. 6b), the ground ($S_{\text{tot}} = 0$) and first excited ($S_{\text{tot}} = 1$) states do not have the same spin quantum number [60]. For this reason, the terms $t_{12}, t_{21} \sim 0$, the transition rates for $"(2, 0)e" \leftrightarrow "(1, 1)g"$ (corresponding to $"(2, 0)\text{T}" \leftrightarrow "(1, 1)\text{S}"$) and $"(2, 0)g" \leftrightarrow "(1, 1)e"$ (corresponding to $"(2, 0)\text{S}" \leftrightarrow "(1, 1)\text{T}"$) are negligible in our setup with $B \ll 1 \text{ mT}$ (see Fig. 6d) [54, 66]. Also, spatial separation of the holes in the $"(1, 1)"$ configuration, results in a negligible exchange splitting between

“(1, 1)g” and “(1, 1)e”, and we set $\Delta_R = 0$ in model Hamiltonian for the even case. Because the number of holes in the left QD is the same as in the odd case, we keep the same value of Δ_L as in the odd case.

The aforementioned Hamiltonian, combined with the generalized input-output theory for a multi-level DQD system interacting with a superconducting resonator (see Supplementary Note 7) [61], reproduces the features observed in the panels of Fig. 5a and Figs. 6a and b. The relevant Hamiltonian parameters are shown in Supplementary Note 8 and Supplementary Note 10.

It is worth noting that a similar model can be applied to investigate a resonator coupled to a generic multi-level DQD system, thus offering opportunities to explore valley-orbit states in silicon coupled to superconducting resonators [67].

5 Data availability

The datasets generated during the current study are available in Zenodo with the identifier <https://doi.org/10.5281/zenodo.13935167>.

References

- [1] Burkard, G., Ladd, T.D., Pan, A., Nichol, J.M., Petta, J.R.: Semiconductor spin qubits. *Rev. Mod. Phys.* **95**(2), 025003 (2023) <https://doi.org/10.1103/RevModPhys.95.025003>
- [2] Takeda, K., Noiri, A., Nakajima, T., Kobayashi, T., Tarucha, S.: Quantum error correction with silicon spin qubits. *Nature* **608**(7924), 682–686 (2022) <https://doi.org/10.1038/s41586-022-04986-6>
- [3] Philips, S.G.J., Madzik, M.T., Amitonov, S.V., de Snoo, S.L., Russ, M., Kalhor, N., Volk, C., Lawrie, W.I.L., Brousse, D., Tryputen, L., Wuetz, B.P., Sammak, A., Veldhorst, M., Scappucci, G., Vandersypen, L.M.K.: Universal control of a six-qubit quantum processor in silicon. *Nature* **609**(7929), 919–924 (2022) <https://doi.org/10.1038/s41586-022-05117-x>
- [4] Hendrickx, N.W., Franke, D.P., Sammak, A., Scappucci, G., Veldhorst, M.: Fast two-qubit logic with holes in germanium. *Nature* **577**(7791), 487–491 (2020) <https://doi.org/10.1038/s41586-019-1919-3>
- [5] Froning, F.N.M., Camenzind, L.C., Molen, O.A.H., Li, A., Bakkers, E.P.A.M., Zumbühl, D.M., Braakman, F.R.: Ultrafast hole spin qubit with gate-tunable spin–orbit switch functionality. *Nat. Nanotechnol.* **16**(3), 308–312 (2021) <https://doi.org/10.1038/s41565-020-00828-6>
- [6] Scappucci, G., Kloeffel, C., Zwanenburg, F.A., Loss, D., Myronov, M., Zhang, J.-J., De Franceschi, S., Katsaros, G., Veldhorst, M.: The germanium quantum information route. *Nat Rev Mater* **6**(10), 926–943 (2021) <https://doi.org/10.1038/s41578-020-00262-z>
- [7] Bulaev, D.V., Loss, D.: Electric Dipole Spin Resonance for Heavy Holes in Quantum Dots. *Physical Review Letters* **98**(9), 097202 (2007) <https://doi.org/10.1103/PhysRevLett.98.097202>
- [8] Bulaev, D.V., Loss, D.: Spin Relaxation and Decoherence of Holes in Quantum Dots. *Physical Review Letters* **95**(7), 076805 (2005) <https://doi.org/10.1103/PhysRevLett.95.076805>
- [9] Voisin, B., Maurand, R., Barraud, S., Vinet, M., Jehl, X., Sanquer, M., Renard, J., De Franceschi, S.: Electrical Control of g-Factor in a Few-Hole Silicon Nanowire MOSFET. *Nano Lett.* **16**(1), 88–92 (2016) <https://doi.org/10.1021/acs.nanolett.5b02920>
- [10] Geyer, S., Hetényi, B., Bosco, S., Camenzind, L.C., Egli, R.S., Fuhrer, A., Loss, D., Warburton, R.J., Zumbühl, D.M., Kuhlmann, A.V.: Two-qubit logic with anisotropic exchange in a fin field-effect transistor (2022) [arxiv:2212.02308](https://arxiv.org/abs/2212.02308) [cond-mat, physics:quant-ph]
- [11] Kloeffel, C., Trif, M., Loss, D.: Strong spin-orbit interaction and helical hole states in Ge/Si nanowires. *Physical Review B* **84**(19), 195314 (2011) <https://doi.org/10.1103/PhysRevB.84.195314>
- [12] Hendrickx, N.W., Lawrie, W.I.L., Russ, M., van Riggelen, F., de Snoo, S.L., Schouten, R.N., Sammak, A., Scappucci, G., Veldhorst, M.: A four-qubit germanium quantum processor. *Nature* **591**(7851), 580–585 (2021) <https://doi.org/10.1038/s41586-021-03332-6>
- [13] Hendrickx, N.W., Lawrie, W.I.L., Petit, L., Sammak, A., Scappucci, G., Veldhorst, M.: A single-hole spin qubit. *Nat Commun* **11**(1), 3478 (2020) <https://doi.org/10.1038/s41467-020-17211-7>
- [14] Stehouwer, L.E.A., Tosato, A., Degli Esposti, D., Costa, D., Veldhorst, M., Sammak, A., Scappucci, G.: Germanium wafers for strained quantum wells with low disorder. *Appl. Phys. Lett.* **123**(9), 092101 (2023) <https://doi.org/10.1063/5.0158262>
- [15] Hendrickx, N.W., Franke, D.P., Sammak, A., Kouwenhoven, M., Sabbagh, D., Yeoh, L., Li, R., Tagliaferri, M.L.V., Virgilio, M., Capellini, G., Scappucci, G., Veldhorst, M.: Gate-controlled quantum dots and superconductivity in planar germanium. *Nature Communications* **9**(2835) (2018) <https://doi.org/10.1038/s41467-018-05299-x>
- [16] Sammak, A., Sabbagh, D., Hendrickx, N.W., Lodari, M., Paquelet Wuetz, B., Tosato, A., Yeoh, L., Bollani, M., Virgilio, M., Schubert, M.A., Zaumseil, P., Capellini, G., Veldhorst, M., Scappucci, G.: Shallow and undoped germanium quantum wells: A playground for spin and hybrid quantum technology. *Advanced Functional Materials* **29**(14), 1807613 (2019) <https://doi.org/10.1002/adfm.201807613> <https://onlinelibrary.wiley.com/doi/pdf/10.1002/adfm.201807613>

- [17] Borsoi, F., Hendrickx, N.W., John, V., Meyer, M., Motz, S., van Riggelen, F., Sammak, A., de Snoo, S.L., Scappucci, G., Veldhorst, M.: Shared control of a 16 semiconductor quantum dot crossbar array. *Nat. Nanotechnol.*, 1–7 (2023) <https://doi.org/10.1038/s41565-023-01491-3>
- [18] van Riggelen-Doelman, F., Wang, C.-A., de Snoo, S.L., Lawrie, W.I.L., Hendrickx, N.W., Rimbach-Russ, M., Sammak, A., Scappucci, G., Déprez, C., Veldhorst, M.: Coherent spin qubit shuttling through germanium quantum dots (2023) [arXiv:2308.02406](https://arxiv.org/abs/2308.02406) [cond-mat, physics:quant-ph]
- [19] Harvey-Collard, P., Dijkema, J., Zheng, G., Sammak, A., Scappucci, G., Vandersypen, L.M.K.: Coherent Spin-Spin Coupling Mediated by Virtual Microwave Photons. *Phys. Rev. X* **12**(2), 021026 (2022) <https://doi.org/10.1103/PhysRevX.12.021026>
- [20] van Woerkom, D.J., Scarlino, P., Ungerer, J.H., Müller, C., Koski, J.V., Landig, A.J., Reichl, C., Wegscheider, W., Ihn, T., Ensslin, K., Wallraff, A.: Microwave Photon-Mediated Interactions between Semiconductor Qubits. *Phys. Rev. X* **8**(4), 041018 (2018) <https://doi.org/10.1103/PhysRevX.8.041018>
- [21] Borjans, F., Croot, X.G., Mi, X., Gullans, M.J., Petta, J.R.: Resonant microwave-mediated interactions between distant electron spins. *Nature* **577**(7789), 195–198 (2020) <https://doi.org/10.1038/s41586-019-1867-y>
- [22] Zheng, G., Samkharadze, N., Noordam, M.L., Kalhor, N., Brousse, D., Sammak, A., Scappucci, G., Vandersypen, L.M.K.: Rapid gate-based spin read-out in silicon using an on-chip resonator. *Nature Nanotechnology* **14**(8), 742–746 (2019) <https://doi.org/10.1038/s41565-019-0488-9>
- [23] Scarlino, P., van Woerkom, D.J., Stockklauser, A., Koski, J.V., Collodo, M.C., Gasparinetti, S., Reichl, C., Wegscheider, W., Ihn, T., Ensslin, K., Wallraff, A.: All-Microwave Control and Dispersive Readout of Gate-Defined Quantum Dot Qubits in Circuit Quantum Electrodynamics. *Physical Review Letters* **122**(20), 206802 (2019) <https://doi.org/10.1103/PhysRevLett.122.206802>
- [24] Kim, C.W., Nichol, J.M., Jordan, A.N., Franco, I.: Analog Quantum Simulation of the Dynamics of Open Quantum Systems with Quantum Dots and Microelectronic Circuits. *PRX Quantum* **3**(4), 040308 (2022) <https://doi.org/10.1103/PRXQuantum.3.040308>
- [25] Khan, W., Potts, P.P., Lehmann, S., Thelander, C., Dick, K.A., Samuelsson, P., Maisi, V.F.: Efficient and continuous microwave photoconversion in hybrid cavity-semiconductor nanowire double quantum dot diodes. *Nature Communications* **12**(1), 5130 (2021) <https://doi.org/10.1038/s41467-021-25446-1>
- [26] Mi, X., Cady, J.V., Zajac, D.M., Deelman, P.W., Petta, J.R.: Strong coupling of a single electron in silicon to a microwave photon. *Science* **355**(6321), 156–158 (2017) <https://doi.org/10.1126/science.aal2469>
- [27] Samkharadze, N., Zheng, G., Kalhor, N., Brousse, D., Sammak, A., Mendes, U.C., Blais, A., Scappucci, G., Vandersypen, L.M.K.: Strong spin-photon coupling in silicon. *Science* **359**(6380), 1123–1127 (2018) <https://doi.org/10.1126/science.aar4054>
- [28] Mi, X., Benito, M., Putz, S., Zajac, D.M., Taylor, J.M., Burkard, G., Petta, J.R.: A coherent spin–photon interface in silicon. *Nature* **555**(7698), 599–603 (2018) <https://doi.org/10.1038/nature25769>
- [29] Scarlino, P., Ungerer, J.H., van Woerkom, D.J., Mancini, M., Stano, P., Müller, C., Landig, A.J., Koski, J.V., Reichl, C., Wegscheider, W., Ihn, T., Ensslin, K., Wallraff, A.: In situ Tuning of the Electric-Dipole Strength of a Double-Dot Charge Qubit: Charge-Noise Protection and Ultrastrong Coupling. *Phys. Rev. X* **12**(3), 031004 (2022) <https://doi.org/10.1103/PhysRevX.12.031004>
- [30] Stockklauser, A., Scarlino, P., Koski, J.V., Gasparinetti, S., Andersen, C.K., Reichl, C., Wegscheider, W., Ihn, T., Ensslin, K., Wallraff, A.: Strong Coupling Cavity QED with Gate-Defined Double Quantum Dots Enabled by a High Impedance Resonator. *Phys. Rev. X* **7**(1), 011030 (2017) <https://doi.org/10.1103/PhysRevX.7.011030>
- [31] Ungerer, J.H., Pally, A., Kononov, A., Lehmann, S., Ridderbos, J., Potts, P.P., Thelander, C., Dick, K.A., Maisi, V.F., Scarlino, P., Baumgartner, A., Schönenberger, C.: Strong coupling between a microwave photon and a singlet-triplet qubit (2023) [arXiv:2303.16825](https://arxiv.org/abs/2303.16825) [cond-mat.mes-hall]
- [32] Yu, C.X., Zihlmann, S., Abadillo-Uriel, J.C., Michal, V.P., Rambal, N., Niebojewski, H., Bedecarrats, T., Vinet, M., Dumur, E., Filippone, M., Bertrand, B., De Franceschi, S., Niquet, Y.-M., Maurand, R.:

- Strong coupling between a photon and a hole spin in silicon **18**(7), 741–746 (2023) <https://doi.org/10.1038/s41565-023-01332-3>
- [33] Kang, Y., Li, Z.-H., Kong, Z.-Z., Li, F.-G., Hao, T.-Y., Wei, Z.-C., Deng, S.-Y., Wang, B.-C., Li, H.-O., Wang, G.-L., Guo, G.-C., Cao, G., Guo, G.-P.: Coupling of Hole Double Quantum Dot in Planar Germanium to a Microwave Cavity. arXiv (2023). <https://doi.org/10.48550/arXiv.2310.08145>
- [34] Wang, R., Deacon, R.S., Sun, J., Yao, J., Lieber, C.M., Ishibashi, K.: Gate Tunable Hole Charge Qubit Formed in a Ge/Si Nanowire Double Quantum Dot Coupled to Microwave Photons. *Nano Letters* **19**(2), 1052–1060 (2019) <https://doi.org/10.1021/acs.nanolett.8b04343>
- [35] Li, Y., Li, S.-X., Gao, F., Li, H.-O., Xu, G., Wang, K., Liu, D., Cao, G., Xiao, M., Wang, T., Zhang, J.-J., Guo, G.-C., Guo, G.-P.: Coupling a Germanium Hut Wire Hole Quantum Dot to a Superconducting Microwave Resonator. *Nano Letters* **18**(3), 2091–2097 (2018) <https://doi.org/10.1021/acs.nanolett.8b00272>
- [36] Hanson, R., Witkamp, B., Vandersypen, L.M.K., Van Beveren, L.H.W., Elzerman, J.M., Kouwenhoven, L.P.: Zeeman Energy and Spin Relaxation in a One-Electron Quantum Dot. *Phys. Rev. Lett.* **91**(19), 196802 (2003) <https://doi.org/10.1103/PhysRevLett.91.196802>
- [37] Golovach, V.N., Khaetskii, A., Loss, D.: Spin relaxation at the singlet-triplet crossing in a quantum dot. *Physical Review B* **77**(4), 045328 (2008) <https://doi.org/10.1103/PhysRevB.77.045328>
- [38] Yannouleas, C., Landman, U.: Symmetry breaking and quantum correlations in finite systems: Studies of quantum dots and ultracold Bose gases and related nuclear and chemical methods. *Reports on Progress in Physics* **70**(12), 2067 (2007) <https://doi.org/10.1088/0034-4885/70/12/R02>
- [39] Abadillo-Uriel, J.C., Martinez, B., Filippone, M., Niquet, Y.-M.: Two-body Wigner molecularization in asymmetric quantum dot spin qubits. *Phys. Rev. B* **104**(19), 195305 (2021) <https://doi.org/10.1103/PhysRevB.104.195305>
- [40] Jang, W., Kim, J., Park, J., Kim, G., Cho, M.-K., Jang, H., Sim, S., Kang, B., Jung, H., Umansky, V., Kim, D.: Wigner-molecularization-enabled dynamic nuclear polarization. *Nat Commun* **14**(1), 2948 (2023) <https://doi.org/10.1038/s41467-023-38649-5>
- [41] Jang, W., Cho, M.-K., Jang, H., Kim, J., Park, J., Kim, G., Kang, B., Jung, H., Umansky, V., Kim, D.: Single-Shot Readout of a Driven Hybrid Qubit in a GaAs Double Quantum Dot. *Nano Lett.* **21**(12), 4999–5005 (2021) <https://doi.org/10.1021/acs.nanolett.1c00783>
- [42] Corrigan, J., Dodson, J.P., Ercan, H.E., Abadillo-Uriel, J.C., Thorgrimsson, B., Knapp, T.J., Holman, N., McJunkin, T., Neyens, S.F., MacQuarrie, E.R., Foote, R.H., Edge, L.F., Friesen, M., Coppersmith, S.N., Eriksson, M.A.: Coherent Control and Spectroscopy of a Semiconductor Quantum Dot Wigner Molecule. *Phys. Rev. Lett.* **127**(12), 127701 (2021) <https://doi.org/10.1103/PhysRevLett.127.127701>
- [43] Pecker, S., Kuemmeth, F., Secchi, A., Rontani, M., Ralph, D.C., McEuen, P.L., Ilani, S.: Observation and spectroscopy of a two-electron Wigner molecule in an ultraclean carbon nanotube. *Nature Phys* **9**(9), 576–581 (2013) <https://doi.org/10.1038/nphys2692>
- [44] Shapir, I., Hamo, A., Pecker, S., Moca, C.P., Legeza, O., Zarand, G., Ilani, S.: Imaging the electronic wigner crystal in one dimension. *Science* **364**(6443), 870–875 (2019) <https://doi.org/10.1126/science.aat0905> <https://www.science.org/doi/pdf/10.1126/science.aat0905>
- [45] Yannouleas, C., Landman, U.: Wigner molecules and hybrid qubits. *J. Phys.: Condens. Matter* **34**(21), 21–01 (2022) <https://doi.org/10.1088/1361-648X/ac5c28>
- [46] Ercan, H.E., Coppersmith, S.N., Friesen, M.: Strong electron-electron interactions in si/sige quantum dots. *Phys. Rev. B* **104**, 235302 (2021) <https://doi.org/10.1103/PhysRevB.104.235302>
- [47] Yannouleas, C., Landman, U.: Molecular formations and spectra due to electron correlations in three-electron hybrid double-well qubits. *Phys. Rev. B* **105**(20), 205302 (2022) <https://doi.org/10.1103/PhysRevB.105.205302>
- [48] Yannouleas, C., Landman, U.: Spontaneous Symmetry Breaking in Single and Molecular Quantum Dots.

Physical Review Letters **82**(26), 5325–5328 (1999) <https://doi.org/10.1103/PhysRevLett.82.5325>

- [49] Li, Y., Yannouleas, C., Landman, U.: Artificial quantum-dot helium molecules: Electronic spectra, spin structures, and Heisenberg clusters. *Physical Review B* **80**(4), 045326 (2009) <https://doi.org/10.1103/PhysRevB.80.045326>
- [50] Szafran, B., Peeters, F.M., Bednarek, S., Chwiej, T., Adamowski, J.: Spatial ordering of charge and spin in quasi-one-dimensional Wigner molecules. *Physical Review B* **70**(3), 035401 (2004) <https://doi.org/10.1103/PhysRevB.70.035401>
- [51] Hetényi, B., Bosco, S., Loss, D.: Anomalous Zero-Field Splitting for Hole Spin Qubits in Si and Ge Quantum Dots. *Phys. Rev. Lett.* **129**(11), 116805 (2022) <https://doi.org/10.1103/PhysRevLett.129.116805>
- [52] Shi, Z., Simmons, C.B., Prance, J.R., Gamble, J.K., Koh, T.S., Shim, Y.-P., Hu, X., Savage, D.E., Lagally, M.G., Eriksson, M.A., Friesen, M., Coppersmith, S.N.: Fast Hybrid Silicon Double-Quantum-Dot Qubit. *Phys. Rev. Lett.* **108**(14), 140503 (2012) <https://doi.org/10.1103/PhysRevLett.108.140503>
- [53] Masluk, N.A., Pop, I.M., Kamal, A., Mineev, Z.K., Devoret, M.H.: Microwave characterization of Josephson junction arrays: Implementing a low loss superinductance. *Phys. Rev. Lett.* **109**, 137002 (2012) <https://doi.org/10.1103/PhysRevLett.109.137002>
- [54] Jirovec, D., Hofmann, A., Ballabio, A., Mutter, P.M., Tavani, G., Botifoll, M., Crippa, A., Kukucka, J., Sagi, O., Martins, F., Saez-Mollejo, J., Prieto, I., Borovkov, M., Arbiol, J., Chrastina, D., Isella, G., Katsaros, G.: A singlet-triplet hole spin qubit in planar Ge. *Nat. Mater.* **20**(8), 1106–1112 (2021) <https://doi.org/10.1038/s41563-021-01022-2>
- [55] Castellanos-Beltran, M.A., Lehnert, K.W.: Widely tunable parametric amplifier based on a superconducting quantum interference device array resonator. *Applied Physics Letters* **91**(8), 083509 (2007) <https://doi.org/10.1063/1.2773988>
- [56] Frey, T., Leek, P.J., Beck, M., Faist, J., Wallraff, A., Ensslin, K., Ihn, T., Büttiker, M.: Quantum dot admittance probed at microwave frequencies with an on-chip resonator. *Phys. Rev. B* **86**(11), 115303 (2012) <https://doi.org/10.1103/PhysRevB.86.115303>
- [57] Wiel, W.G., De Franceschi, S., Elzerman, J.M., Fujisawa, T., Tarucha, S., Kouwenhoven, L.P.: Electron transport through double quantum dots. *Rev. Mod. Phys.* **75**, 1–22 (2002) <https://doi.org/10.1103/RevModPhys.75.1>
- [58] Clerk, A.A., Lehnert, K.W., Bertet, P., Petta, J.R., Nakamura, Y.: Hybrid quantum systems with circuit quantum electrodynamics. *Nature Physics* **19**(3), 257–267 (2020) <https://doi.org/10.1038/s41567-020-0797-9>
- [59] Shi, Z., Simmons, C.B., Ward, D.R., Prance, J.R., Wu, X., Koh, T.S., Gamble, J.K., Savage, D.E., Lagally, M.G., Friesen, M., Coppersmith, S.N., Eriksson, M.A.: Fast coherent manipulation of three-electron states in a double quantum dot. *Nat Commun* **5**(1), 3020 (2014) <https://doi.org/10.1038/ncomms4020>
- [60] Johnson, A.C., Petta, J.R., Marcus, C.M., Hanson, M.P., Gossard, A.C.: Singlet-triplet spin blockade and charge sensing in a few-electron double quantum dot. *Physical Review B* **72**(16), 165308 (2005) <https://doi.org/10.1103/PhysRevB.72.165308>
- [61] Burkard, G., Petta, J.R.: Dispersive readout of valley splittings in cavity-coupled silicon quantum dots. *Physical Review B* **94**(19), 195305 (2016) <https://doi.org/10.1103/PhysRevB.94.195305>
- [62] Müller, C., Cole, J.H., Lisenfeld, J.: Towards understanding two-level-systems in amorphous solids: insights from quantum circuits. *Reports on Progress in Physics* **82**(12), 124501 (2019) <https://doi.org/10.1088/1361-6633/ab3a7e>
- [63] Abadillo-Uriel, J.C., King, E., Coppersmith, S.N., Friesen, M.: Long-range two-hybrid-qubit gates mediated by a microwave cavity with red sidebands. *Physical Review A* **104**(3), 032612 (2021) <https://doi.org/10.1103/PhysRevA.104.032612>
- [64] Paladino, E., Galperin, Y.M., Falci, G., Altshuler, B.L.: $1/f$ noise: Implications for solid-state quantum information. *Rev. Mod. Phys.* **86**(2), 361–418 (2014) <https://doi.org/10.1103/RevModPhys.86.361>

- [65] Thorgrimsson, B., Kim, D., Yang, Y.-C., Smith, L.W., Simmons, C.B., Ward, D.R., Foote, R.H., Corrigan, J., Savage, D.E., Lagally, M.G., Friesen, M., Coppersmith, S.N., Eriksson, M.A.: Extending the coherence of a quantum dot hybrid qubit. *npj Quantum Inf* **3**(1), 1–4 (2017) <https://doi.org/10.1038/s41534-017-0034-2>
- [66] Nichol, J.M., Harvey, S.P., Shulman, M.D., Pal, A., Umansky, V., Rashba, E.I., Halperin, B.I., Yacoby, A.: Quenching of dynamic nuclear polarization by spin–orbit coupling in GaAs quantum dots. *Nat Commun* **6**(1), 7682 (2015) <https://doi.org/10.1038/ncomms8682>
- [67] Borjans, F., Zhang, X., Mi, X., Cheng, G., Yao, N., Jackson, C.A.C., Edge, L.F., Petta, J.R.: Probing the Variation of the Intervalley Tunnel Coupling in a Silicon Triple Quantum Dot. *PRX Quantum* **2**(2), 020309 (2021) <https://doi.org/10.1103/PRXQuantum.2.020309>

Acknowledgements

The authors thank Simone Frasca, Vincent Jouanny, Guillaume Beaulieu, Camille Roy, Dominic Dahinden, Davide Lombardo, Daniel Chrastina and Siddhart Gautam for contributing in some cleanroom fabrication steps, the measurement setup, device simulations, data analysis and for the useful discussions.

P.S. acknowledges support from the Swiss National Science Foundation (SNSF) through the grants Ref. No. 200021_200418 and Ref. No. 206021_205335, and from the Swiss State Secretariat for Education, Research and Innovation (SERI) under contract number 01042765 SEFRI MB22.00081. W.J. acknowledges support from EPFL QSE Postdoctoral Fellowship Grant. S.B, D.L and P.S acknowledge support from the NCCR Spin Qubit in Silicon (NCCR-SPIN) Grant No. 51NF40-180604. M.J., G.K., G.I. and S.C. acknowledge support from the Horizon Europe Project IGNITE ID 101070193. G.K. acknowledges support from the FWF via the P32235 and I05060 projects.

Contributions

F.D.P., F.O., W.J. and P.S. conceived the project. F.D.P. and F.O. fabricated the device and built the experimental setup. F.D.P., F.O. developed the fabrication recipe with inputs from M.J. and G.K.. F.D.P., F.O. and M.J. designed the hybrid device. F.D.P., F.O. and W.J. performed the electrical measurements and analyzed the data. W.J. and S.B. derived the theoretical model and simulated the strongly correlated states. G.I. and S.C. designed the SiGe heterostructure and performed the growth. P.S., D.L. and G.K. initiated the project. P.S., D.L. supervised the project. F.D.P., F.O., W.J. and P.S. wrote the manuscript with inputs from the authors. F.D.P., F.O., W.J. contributed equally to this work.

Competing interests

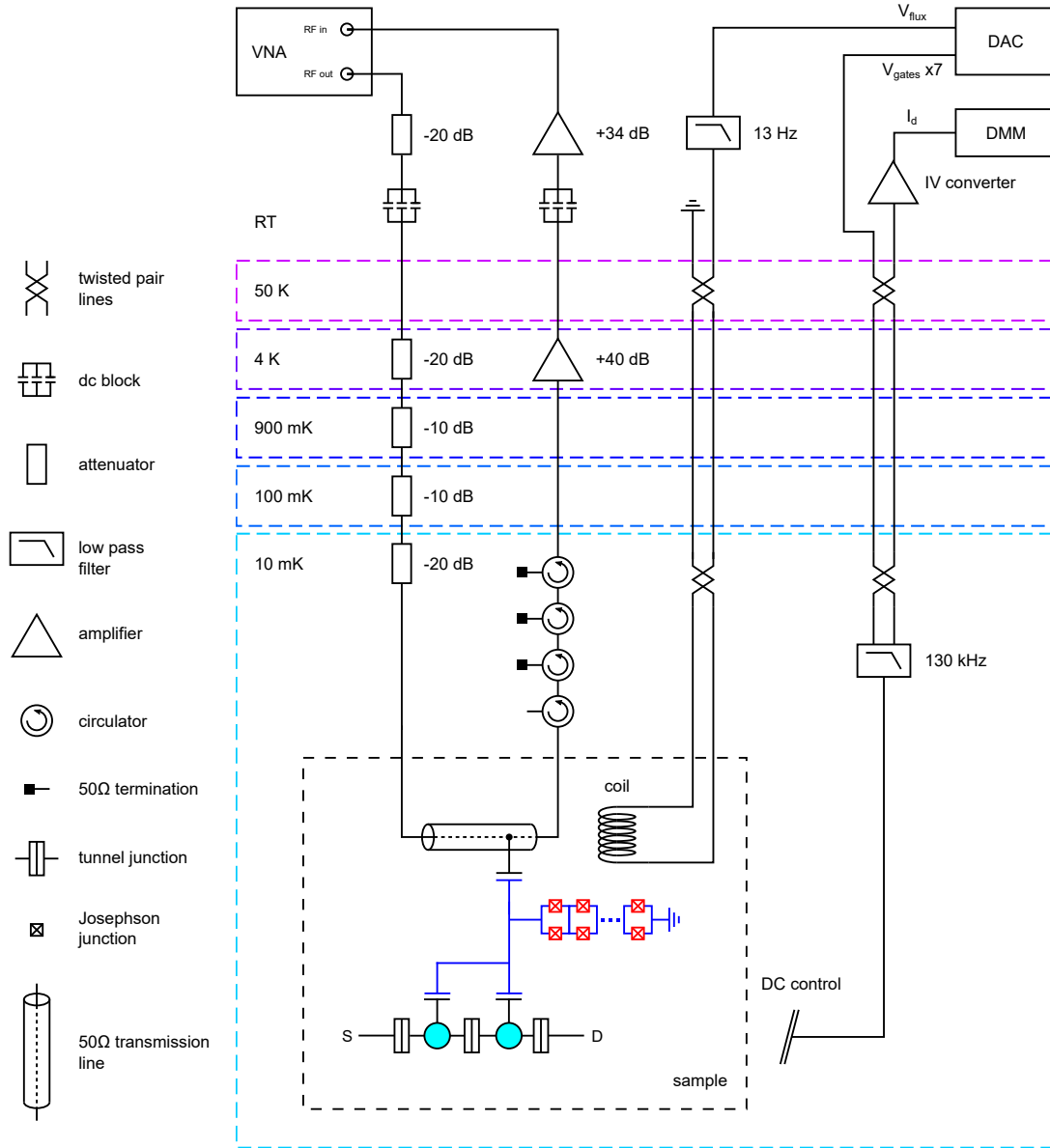
The authors declare no competing interests.

Supplementary Information: Strong hole-photon coupling in planar Ge for probing charge degree and strongly-correlated states

Contents

1	Experimental Setup	24
2	Stability diagrams and number of charges estimation	26
3	Cavity characterization	28
4	Input-output theory for charge qubits	30
5	Charge qubit spectroscopies	32
6	Coulomb interactions in doubly occupied QDs and WM formations	34
7	Input-output theory for strongly-correlated states	35
8	Spectroscopies of the strongly-correlated states	37
9	DC transport measurements in the even and odd hole configurations	39
10	Simulations of spectroscopies in Fig. 6	41

1 Experimental Setup

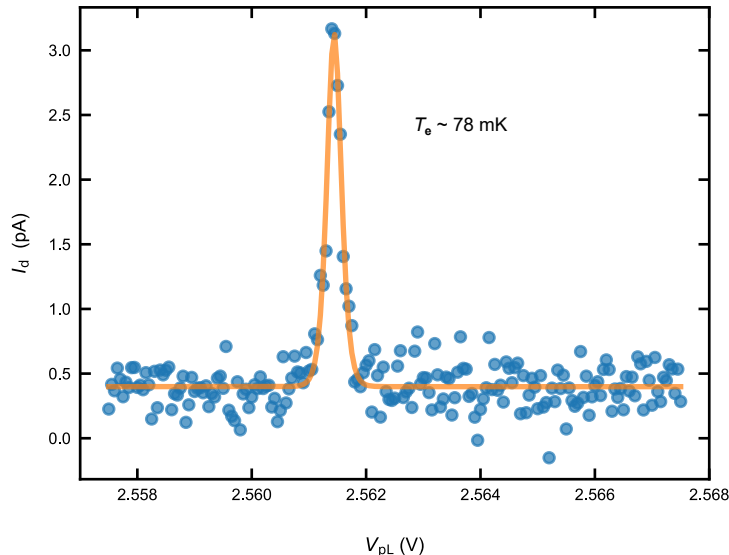


Supplementary Figure 1 Schematic of cryogenic and room temperature measurement setup.

The measurements reported in this work are performed in a dilution refrigerator (Bluefors LD250) at base temperatures around 10 mK (see Supplementary Figure 1). The device is mounted on a printed circuit board (PCB, QDevil QBoard), which consists of a motherboard with an RC low pass filtering stage (130 kHz cut-off) and a daughterboard that hosts the device. Good contact between daughter- and motherboard is ensured by spring contacts. The coaxial cables for RF signals are connected directly to the daughterboard.

Gate and bias voltages for the QDs are generated by a 24-channel digital-to-analog converter (DAC, QDevil QDAC-II) and are passed to the sample via twisted pair cables made of phosphor bronze and the RC filtering stage (65 kHz cut-off) on the QBoard. The drain current through the device is measured by a digital multimeter (DMM, Keysight 34465A) after being amplified by an IV converter (Basel Precision Instruments SP 983C). The magnetic flux of the SQUID array resonator is controlled by a small superconducting coil mounted directly above the sample. The coil bias voltage is generated by a DAC (QDevil QDAC-II) and passes through an RC low pass filter (13 Hz cut-off) at room temperature with a total resistance of 1 kΩ followed by superconducting twisted pair lines that are connected to the coil.

Resonator spectroscopy is performed with a vector network analyzer (VNA, Rohde & Schwarz ZNB20). The VNA output is attenuated at room temperature, followed by a dc block (Inmet 8039 inner-outer). The signal passes through an attenuation chain before reaching the $50\ \Omega$ coplanar waveguide (CPW) transmission line on the device. The transmitted signal then passes through a chain of two circulators (Low Noise Factory CICIC4.8A) and two isolators (Low Noise Factory ISISC4.8A). The third port of the second circulator is terminated, effectively acting as another isolator. The signal is amplified by a HEMT at the 4 K stage (Low Noise Factory LNC4.8C) and by a low noise amplifier at room temperature (Agile AMT.A0284) after passing through another dc block (Inmet 8039).



Supplementary Figure 2 Electron temperature measurement via Coulomb oscillation. Charge transition line of the left QD recorded with dc-current measurement. Numerical fit to a model (solid orange line, Supplementary Eq. 3) results in electron temperature $T_e \sim 78$ mK.

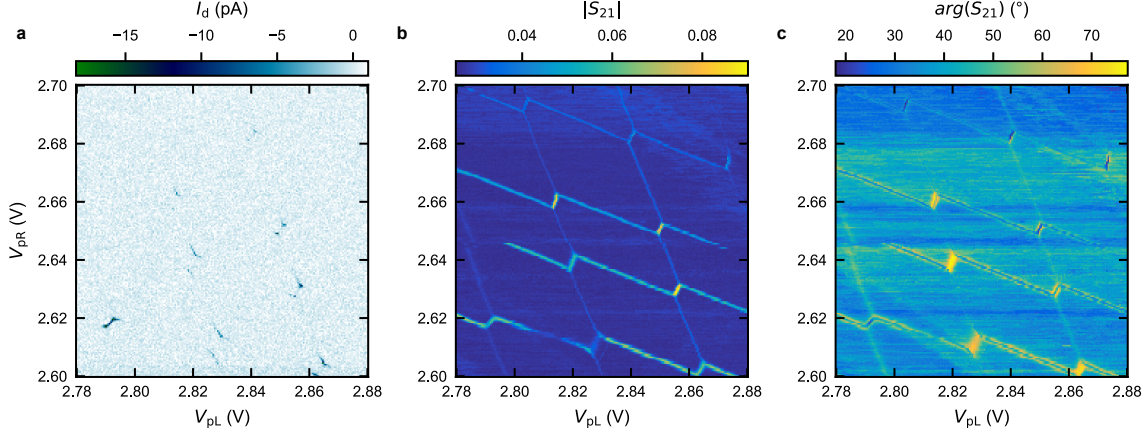
The electron temperature is extracted by measuring Coulomb oscillations. When the dot-reservoir tunneling rate Γ_r is low enough, such that $\Gamma_r < 4k_B T_e$, where k_B is the Boltzmann constant and T_e is the temperature of the reservoirs, the line shape of the Coulomb peak can be approximated by [1]

$$G(T_e) = \frac{G_{\max}}{\cosh\left(\frac{\alpha(V_g - V_0)}{2k_B T_e}\right)^2} + c, \quad (3)$$

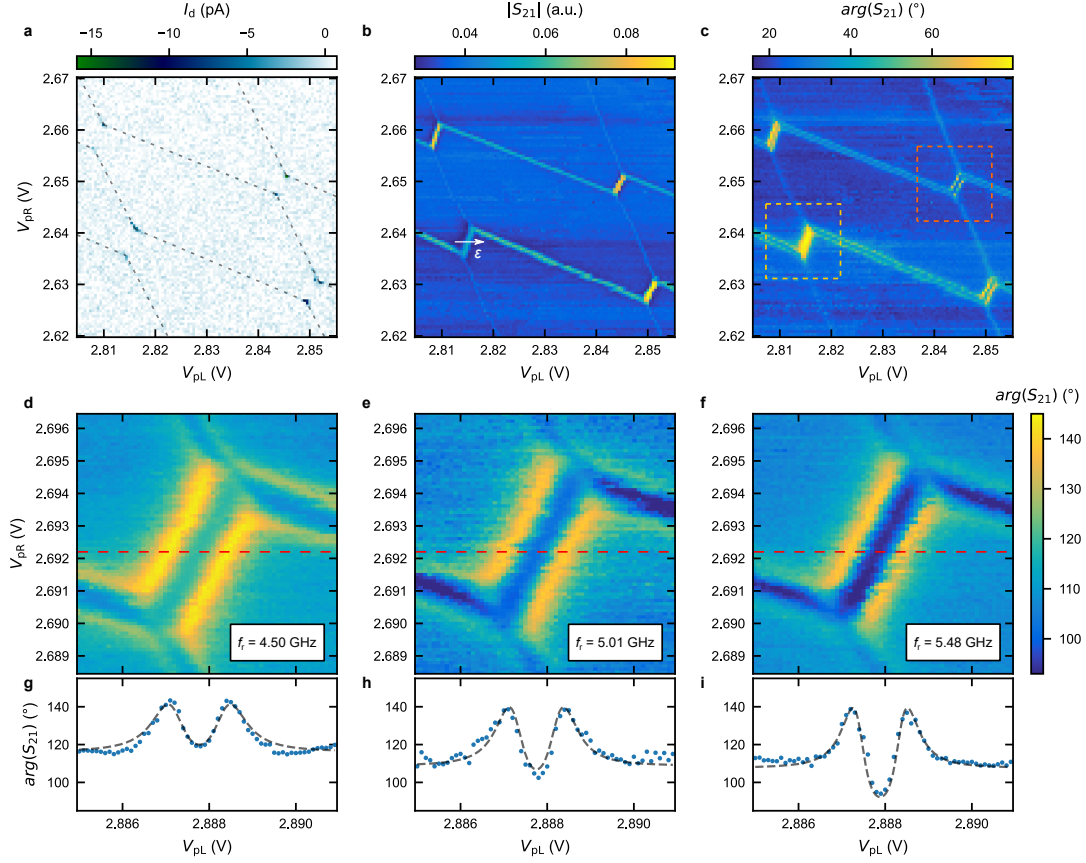
where $\alpha = 80$ meV/V is the gate lever arm, V_g is the gate voltage, $V_0 = E_F/\alpha$ is the gate voltage where the dot level aligns with the Fermi energy of the leads and c is a constant offset. Fitting the measured current I_d to $V_{\text{bias}}G(T_e)$ yields an effective electron temperature of $T_e \sim 78$ mK (see Supplementary Figure 2).

2 Stability diagrams and number of charges estimation

Due to the relatively large size of our dots, they cannot be depleted to the single hole regime within a practical gate voltage range. As a consequence, getting a precise particle number is not straightforward. In this regard, we first present an upper bound of this number based on the saturation carrier density measured when the channel is fully conductive, $p_0 = 7.54 \cdot 10^{11} \text{ cm}^{-2}$. Based on the QD anisotropy ~ 0.8 (see Supplementary Note 6) and QD radius $l_{\text{QD}} \sim 70 \text{ nm}$ (extracted from Coulomb diamond measurements, see Supplementary Note 6), we obtain a QD area $\sim 12000 \text{ nm}^2$, which results in a maximum charge number of ~ 90 . We note, however, that the percolation density of the heterostructure may provide more precise estimate of the charge number within, as the QDs are formed when the channel is not fully conductive. While the exact percolation density of our material is not measured, we roughly estimate the percolation density to be $\sim 0.1p_0 - 0.3p_0$ from the previous literature [2–6], which results in a more realistic estimate of the charge number $\sim 9 - 27$.



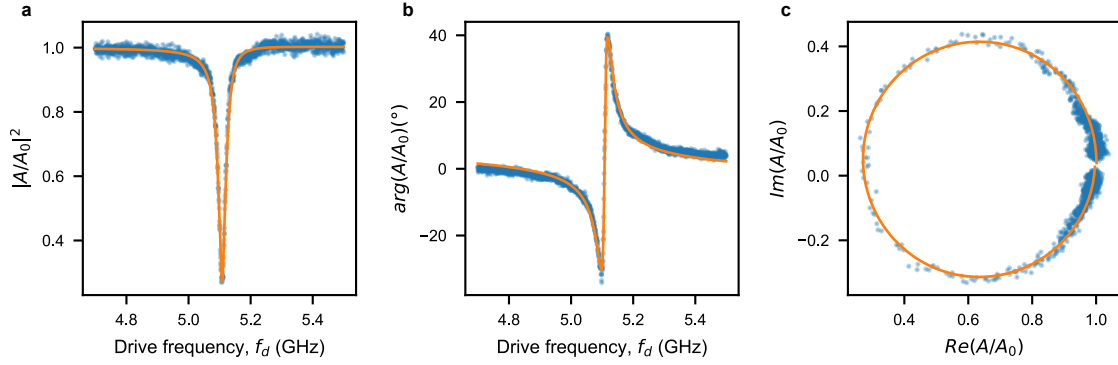
Supplementary Figure 3 Zoom-out charge stability diagram. The DQD charge stability diagram, showing the canonical honeycomb pattern [7], is measured by dc transport (a) through the DQD, as well as detecting magnitude (b) and phase (c) of the feedline transmission S_{21} (at $f_d = f_r = 5.01 \text{ GHz}$), as a function of the applied plunger gate voltages V_{pL} and V_{pR} .



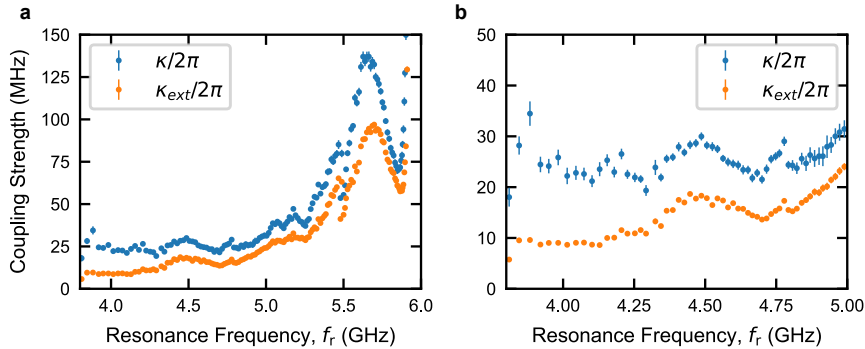
Supplementary Figure 4 Extension to Fig. 2 of the main text. A region of the DQD charge stability diagram as a function of the applied plunger gate voltages V_{pR} and V_{pL} , recorded by dc-transport (a) and by measuring amplitude (b) and phase (c) of the feedline transmission S_{21} at $f_d = f_r = 5.01$ GHz. The resonator detects inter-dot and reservoir-dot transitions when their tunneling rates are close to f_r [8]. Yellow (orange) dashed box in c: The phase signal increases (decreases) near the inter-dot region with respect to the background, if the resonator is dispersively shifted to lower (higher) frequency. Notably, because the resonator gate lever arm is larger for the right QD, the resonator is more sensitive to its QD-reservoir transitions with respect to those of the left QD. **d-f**, Same inter-dot transition probed with $f_r = 4.50$ GHz $< 2t_c/h$ (d), $f_r = 5.01$ GHz $\sim 2t_c/h$ (e) and $f_r = 5.48$ GHz $> 2t_c/h$ (f). The corresponding line-cuts, taken along the red dashed lines, are shown in **g**, **h**, and **i** respectively. The black dashed curves show the simultaneous fit to a master equation (see Methods). Panels **a**, **c**, **e** and **h** correspond to Figs. 2a - d in the main text, respectively.

3 Cavity characterization

The superconducting cavity consists of a quarter-wave high-impedance SQUID array resonator. On one side, it is coupled to a 50Ω waveguide via a coupling capacitance of $C_{\text{ext}} \sim 4$ fF and galvanically connected to the Al ground plane on the other side. The resonator has an equivalent lumped capacitance to ground of $C_{\text{gnd}} = 17$ fF [9]. The total lumped equivalent capacitance of the resonator is $C_r \sim 24$ fF, taking into account the parasitic capacitance of the gate lines, estimated to be ~ 3 fF from static simulations. The inductance of a single SQUID, extracted from room temperature resistance measurements [10], is $L_{\text{SQUID}} \sim 0.63$ nH/SQUID. The total lumped equivalent inductance is $L_r \sim 16$ nH at zero flux. The resulting bare resonance frequency is $f_r \sim 8.0$ GHz. However, the resonator is operated only from 4 to 6 GHz in the experiments reported in this work. In this frequency range, the resonator lumped equivalent impedance $Z_r = \sqrt{L_r/C_r}$ ranges from 1.6 k Ω (at $f_r = 4$ GHz) to 1.1 k Ω (at $f_r = 6$ GHz) and the external coupling rate $\kappa_{\text{ext}}/2\pi$ from 8 MHz to 80 MHz, probably due to the presence of strong standing waves coupled to the resonator around (and above) 6 GHz. The internal loss rate of the resonator $\kappa_{\text{int}}/2\pi$ decreases, below 5 GHz and at low photon numbers ($n_{\text{avg}} \ll 1$), to approximately 9 MHz, allowing the resonator to operate in the overcoupled regime in the majority of the explored frequency range [11]. At $f_r = 5.109$ GHz, roughly in the centre of the frequency operation window, a fit to the master equation of the bare normalized complex feedline transmission, with the charge qubit far detuned, (see Supplementary Eq. (8) in Supplementary Note 4), gives $\kappa/2\pi = 39$ MHz, $\kappa_{\text{ext}}/2\pi = 29$ MHz, $\kappa_{\text{int}}/2\pi = 10$ MHz and $n_{\text{avg}} \sim 0.1$, for a drive power at the resonator input $P_{\text{in}} \sim -136$ dBm. The plots of the resulting normalized amplitude $|A/A_0|^2$, phase $\arg(A/A_0)$ and complex circle, with the aforementioned fitted parameters, are reported in Supplementary Figure 5, where the orange lines represent the fit of the experimental data (blue dots). A more detailed study of the evolution of the external and total coupling strengths κ_{ext} and κ as a function of f_r can be found in Supplementary Figure 6, where the same fit was performed for different flux voltages.



Supplementary Figure 5 Bare cavity characterization. Normalized amplitude $|A/A_0|^2$ (a), phase $\arg(A/A_0)$ (b) and complex circle (c) of the feedline transmission as a function of drive frequency f_d with the charge qubit far detuned from the resonator. Blue dots are experimental data, whereas the orange lines are fits to the master equation.

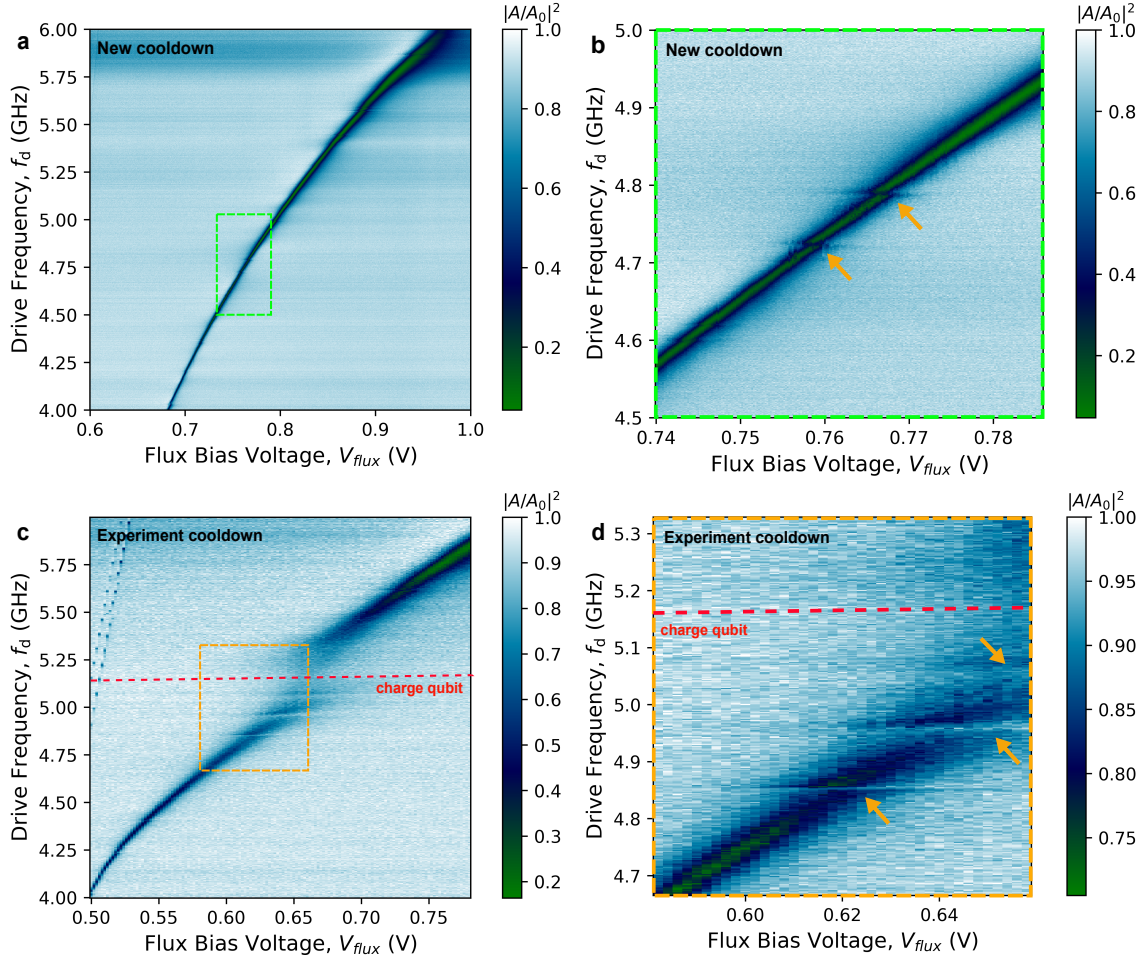


Supplementary Figure 6 Resonator coupling strengths as a function of f_r . a, Loaded (κ) and external (κ_{ext}) coupling strengths of the bare resonator as function of f_r extracted from fitting frequency line-cuts of a flux sweep measurement. The large increase of κ_{ext} towards 6 GHz is attributed to coupling to a standing wave. b, Zoom-in of a to the most interesting frequency range for the presented experiments.

Some of the spectroscopies reported in this work show some extra narrow transitions (Fig. 4a top panel, Fig. 5a top panel and Fig. 6a third panel from the top). To clarify the nature of these extra transitions, we acquire the

resonator response as a function of the magnetic flux with all the gate lines grounded, i.e. with no charge qubit defined. The result is reported in Supplementary Figure 7a. With a careful look at the high-resolution spectrum, many avoided crossings can be observed, as clearly indicated by the orange arrows in the zoom-in reported in Supplementary Figure 7b. We attribute them to the coupling of the high-impedance resonator to two-level systems (TLSs) located in the tunneling junctions [12]. A high-power magnetic flux sweep, not reported here, shows the disappearance of the avoided crossings, indicating a saturation of the TLSs and further supporting our hypothesis. We note that these TLS modes may interact with the qubit mediated by the resonator, which may result in a weak DQD detuning dependence in the spectrum, such as the ones observed in Figs. 5a (top panel) and 6a (third panel from top) in the main manuscript.

The measurements shown in Supplementary Figures 7a and b, however, were acquired in a new cooldown and for this reason some of these avoided crossings appear at different frequencies with respect to the reported measurements. We thus report the same flux sweep in Supplementary Figure 7c, together with the corresponding zoomed-in curve (orange box) in Supplementary Figure 7d, but taken in the same cooldown of the experiments reported in our work. Here, a charge qubit is hybridizing with the resonator at ~ 5.2 GHz to result in vacuum-Rabi mode splitting (red dashed line in Supplementary Figures 7c and d). Also in this case, several avoided crossings are visible, both above and below the charge qubit frequency. This strongly suggests that these extra transitions cannot be attributed to extra states in the DQD, but most likely are due to TLSs in the SQUID array resonator. In the zoom-in of Supplementary Figure 7d, three avoided crossings are clearly visible. The two around 5 GHz correspond to those observed in Fig. 6a (third panel from the top). The highest frequency avoided crossing matches the one visible in Fig. 4a (top panel).



Supplementary Figure 7 Observation of the spurious two-level systems in the SQUID array resonator. **a**, Normalized feedline transmission $|A/A_0|^2$ as a function of the resonator drive frequency f_d and flux voltage V_{flux} with a charge qubit far detuned from the resonator. The measurement is taken with a low photon number ($n_{ph} \ll 1$). **b**, Zoom-in of the green-box region in **a**. Orange arrows denote the signatures of two-level systems (TLSs) interacting with the resonator. **c**, $|A/A_0|^2$ as a function of f_d and V_{flux} with the DQD charge qubit in resonance with the resonator at ~ 5.2 GHz (red dashed line). **d** Zoom-in of the orange box region in **c**. Orange dashed lines denote the signatures of TLSs, unrelated to the DQD charge qubit. **c** is taken in the same cooldown together with the datasets presented in the manuscript, while **a** is taken in a separate cooldown.

4 Input-output theory for charge qubits

The analytic derivation of the resonator response follows the standard procedure of combining the Heisenberg-Langevin equation of motion for the cavity field operator a with the input-output relation [13]. For a bare hanger resonator, in a frame rotating with the driving frequency, the equation of motion reads [14]:

$$\dot{a} = -i\Delta_r a - \frac{\kappa_{\text{ext}} + \kappa_{\text{int}}}{2} a - \sqrt{\frac{\kappa_{\text{ext}}}{2}} b_{\text{in}}, \quad (4)$$

where Δ_r is the resonator-drive detuning $\omega_r - \omega_d$, κ_{ext} is the total coupling strength of the cavity to the b modes of the waveguide, κ_{int} is the internal resonator dissipation and b_{in} is the input field. The steady-state solution of the cavity field ($\dot{a} = 0$) is easily found:

$$a = \frac{-\sqrt{\kappa_{\text{ext}}/2}}{i\Delta_r + \kappa/2} b_{\text{in}}, \quad (5)$$

with $\kappa = \kappa_{\text{ext}} + \kappa_{\text{int}}$, and combined with the input-output relation: $b_{\text{out}} = b_{\text{in}} + \sqrt{\frac{\kappa_{\text{ext}}}{2}} a$ [13] to get the scattering coefficient:

$$S_{21} = \frac{b_{\text{out}}}{b_{\text{in}}} = 1 + \frac{\kappa_{\text{ext}}/2}{i\Delta_r + \kappa/2} = \frac{\Delta_r - i\kappa_{\text{int}}/2}{\Delta_r - i\kappa/2}. \quad (6)$$

The measured resonator response, however, can deviate from the ideal case because of environmental factors and/or impedance mismatches in proximity of the resonator or between input and output ports [15]. The environment is usually modeled with the complex term:

$$ae^{i\alpha} e^{-2\pi i f_d \tau}, \quad (7)$$

where a (α) is a rescaling amplitude (phase shift), τ is the electric delay due to the cable length and f_d the drive frequency. Impedance mismatches are taken into account by a complex $\kappa_{\text{ext}} = |\kappa_{\text{ext}}| e^{i\phi}$, resulting in the corrected scattering coefficient:

$$S_{21} = ae^{i\alpha} e^{-2\pi i f_d \tau} \frac{\Delta_r - i(\kappa - |\kappa_{\text{ext}}| e^{i\phi})/2}{\Delta_r - i\kappa/2}. \quad (8)$$

In the aforementioned experiments, a charge qubit is coupled to the superconducting resonator. The charge qubit Hamiltonian can be written as $H_{\text{cq}} = \frac{\varepsilon}{2} \sigma_z + t_c \sigma_x$, with the DQD detuning ε , the inter-dot tunneling coupling t_c and the Pauli operators σ_x and σ_z . The general resonator-charge qubit Hamiltonian is expressed as

$$H/\hbar = \omega_r a^\dagger a + \frac{\omega_q}{2} \sigma_z + g_{\text{eff}} \sigma_x (a + a^\dagger), \quad (9)$$

where $\omega_r/2\pi$ ($\omega_q/2\pi = \sqrt{\varepsilon^2 + 4t_c^2}/h$) is the resonator (qubit) frequency, $g_{\text{eff}} = g_0 \frac{2t_c}{\hbar\omega_q}$ is the effective charge-photon coupling strength with g_0 representing the coupling strength at $\varepsilon = 0$ and a (a^\dagger) is the photon annihilation (creation) operator. Here, we focus only on transversal interactions $\sigma_x(a + a^\dagger)$, i.e. through the DQD detuning degree of freedom ε , because purely longitudinal interactions ($\sigma_z(a + a^\dagger)$) do not leave spectroscopic signatures. A unitary transformation $U = \exp[-i\omega_d t(a^\dagger a + \sigma_z/2)]$ allows us to rewrite the Hamiltonian in the drive frame (ω_d), using the rotating wave approximation to neglect fast rotating terms:

$$H_{\text{RWA}} = \Delta_r a^\dagger a + \frac{\Delta_q}{2} \sigma_z + g_{\text{eff}} (a^\dagger \sigma_- + a \sigma_+), \quad (10)$$

with Δ_q being the qubit-drive detuning $\omega_q - \omega_d$ and σ_+ and σ_- the qubit raising and lowering operators. The result is the well-known Jaynes-Cummings Hamiltonian. Due to the qubit-resonator interaction, the Heisenberg-Langevin equation of motion for the cavity field a shows an extra term ($[a, g_{\text{eff}}(a^\dagger \sigma_- + a \sigma_+)]$):

$$\dot{a} = -i\Delta_r a - \frac{\kappa_{\text{ext}} + \kappa_{\text{int}}}{2} a - \sqrt{\frac{\kappa_{\text{ext}}}{2}} b_{\text{in}} - ig_{\text{eff}} \sigma_-. \quad (11)$$

The steady-state solution for the cavity field requires the knowledge of σ_- . The time evolution of the qubit lowering operator is again captured by the Heisenberg picture:

$$\dot{\sigma}_- = -i\Delta_q \sigma_- - \Gamma \sigma_- - ig_{\text{eff}} \sigma_z a, \quad (12)$$

with Γ the qubit decoherence rate (including both relaxation and dephasing). Assuming the qubit to be in a thermal state, the expectation value of σ_z can be expressed as the average probability for the qubit to be in the ground (p_0) or in the excited (p_1) state as:

$$\langle \sigma_z \rangle = p_0 - p_1 = \tanh(\hbar\omega_q/k_B T), \quad (13)$$

where k_B is the Boltzmann constant and T the “experimental” temperature, i.e. the temperature of any kind of bath (phonons, traps, reservoirs, etc.) that can exchange thermal energy with the qubit. In the experiment ($\omega_q > 3$ GHz), for $T \approx 10$ mK, $\langle \sigma_z \rangle \approx p_0$, i.e. thermal excitations can be neglected and the qubit is always in the ground state when not driven. Inserting Supplementary Eq. (13) into Supplementary Eq. (12) and setting $\dot{\sigma}_- = 0$ results in the expectation value of the qubit lowering operator:

$$\sigma_- = \frac{g_{\text{eff}} a}{-\Delta_q + i\Gamma}. \quad (14)$$

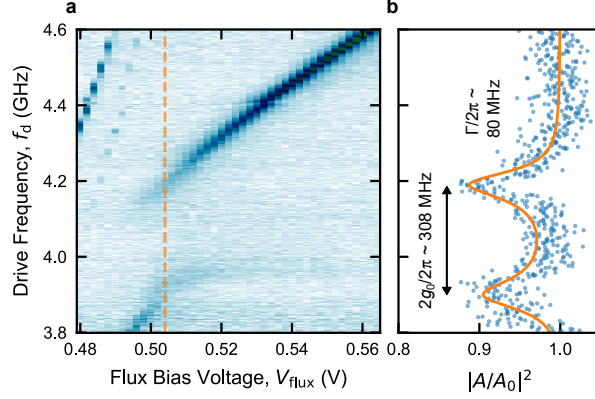
Inserting Supplementary Eq. (14) into Supplementary Eq. (11) and setting $\dot{a} = 0$, the cavity field in the hybridized case is obtained:

$$a = \frac{-\sqrt{\kappa_{\text{ext}}/2}}{i\Delta_r + \kappa/2 + \frac{ig_{\text{eff}}^2}{-\Delta_q + i\Gamma}} b_{\text{in}}. \quad (15)$$

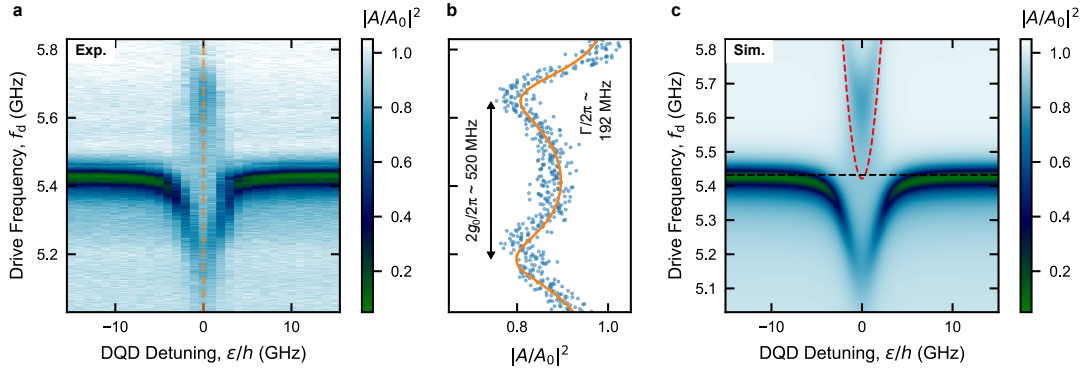
Finally, introducing the DQD susceptibility $\chi = \frac{\sigma_-}{a} = \frac{g_{\text{eff}}}{-\Delta_q + i\Gamma}$ and following the same steps of Supplementary Eq. (6), the expression of S_{21} for the hybridized system is found, including the correction factors for the environment:

$$S_{21} = a e^{i\alpha} e^{-2\pi i f_d \tau} \frac{\Delta_r - i(\kappa - |\kappa_{\text{ext}}| e^{i\phi})/2 + g_{\text{eff}} \chi}{\Delta_r - i\kappa/2 + g_{\text{eff}} \chi}. \quad (16)$$

5 Charge qubit spectroscopies



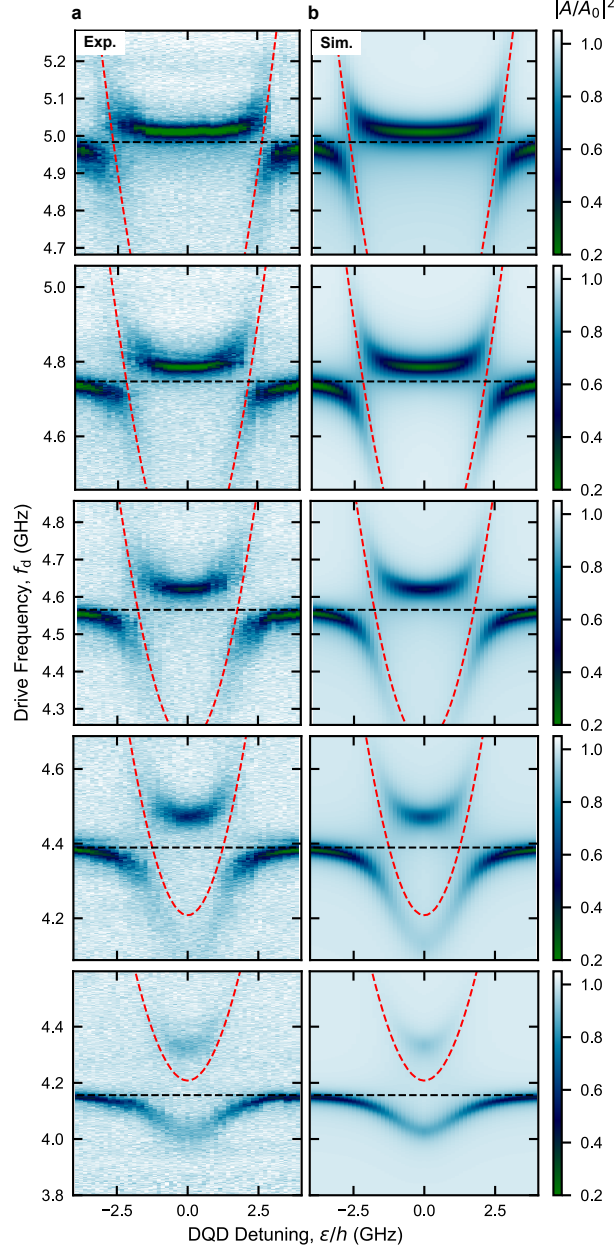
Supplementary Figure 8 Extension to Fig. 3 of the main text. **a**, Normalized amplitude of feedline transmission $|A/A_0|^2$ as a function of drive frequency f_d and the voltage V_{flux} applied to the resonator coil which tunes the resonator frequency f_r . During the measurement, the DQD is kept at $\varepsilon = 0$. An avoided crossing is observed around $V_{\text{flux}} = 504$ mV, when the bare resonator frequency f_r matches the DQD charge transition ($f_r = f_q = 2t_c/h$). **b**, Frequency line-cut at the avoided crossing along the orange dashed line in **a**. A fit to the master equation model is represented by a solid orange line (see Methods). The extracted values for $2g_0$ and Γ are reported in Supplementary Table 1 ($2t_c/h = 4.036$ GHz).



Supplementary Figure 9 Strong charge-photon coupling at the charge sweet spot. **a**, Normalized amplitude of feedline transmission $|A/A_0|^2$ as a function of drive frequency f_d and DQD detuning ε . An avoided crossing - the signature of the strong coupling regime - is observed when the DQD-charge transition matches the bare resonator frequency. **b**, Frequency line-cut (along the orange dashed line in **a**) at resonance, highlighting the vacuum-Rabi splitting $2g_0/2\pi$. A numerical fit to the master equation model is represented by a solid orange line. The extracted values for $2g_0$ and Γ are indicated ($2t_c/h = 5.433$ GHz) and reported in Supplementary Table 1. **c**, Simulation of $|A/A_0|^2$ using input-output theory with the parameters extracted (see Supplementary Table 1) by fitting the dataset in panel **b** to the master equation model (see Methods).

Parameter	Supplementary Figure 8b	Fig. 3c	Supplementary Figure 9b
t_c/h (GHz)	2.018	2.072	2.712
f_r (GHz)	4.052	4.149	5.432*
$g_0/2\pi$ (MHz)	154	165	260
$\Gamma/2\pi$ (MHz)	80	57	192
$\kappa^*/2\pi$ (MHz)	23	19	61
$\kappa_{\text{ext}}^*/2\pi$ (MHz)	9	8	42
C	52	100	23

Supplementary Table 1 Extracted parameters from the three hybrid system configurations shown in Fig. 3. The parameters denoted with * are obtained from a separate measurement of the bare resonator and used as fixed parameters in the master equation fit. The discrepancy between the parameters extracted by V_{flux} (Fig. 3b) and sweeping ε (Figs. 3c) is attributed to a jump of the charge qubit to a slightly higher qubit frequency and to the shorter integration time used for the latter measurement.



Supplementary Figure 10 Detailed spectroscopy of the charge qubit. **a**, Normalized amplitude of feedline transmission $|A/A_0|^2$ as a function of drive frequency f_d and DQD detuning ϵ for five different resonator frequencies (for a constant DQD t_c), revealing the charge qubit dispersion relation. The black (red) dashed line represents bare resonator (DQD-charge qubit excitation) frequency, obtained using the extracted fitting parameters. Some of these datasets are already presented in Fig. 4 in the main text. **b**, Simulation of the normalized amplitude of feedline transmission $|A/A_0|^2$ using input-output theory with the parameters reported in Supplementary Table 2.

Parameter	Panel 1	Panel 2	Panel 3	Panel 4	Panel 5
f_r (GHz)	4.156	4.389	4.565	4.747	4.983
$g_0/2\pi$ (MHz)	155	147	150	148	151
$\kappa^*/2\pi$ (MHz)	19	20	22	32	37
$\kappa_{\text{ext}}^*/2\pi$ (MHz)	8	11	13	21	22

Supplementary Table 2 Extracted individual fitting parameters from the five hybrid system configurations shown in Supplementary Figure 10 numbered from bottom to top. The fitted values for the shared parameters are $t_c/h = 2.104$ GHz, $\beta_{\text{pL}} = 23.8$ meV/V, $\Gamma_0 = 57$ MHz, $\Gamma_\epsilon = 164$ MHz. The parameters denoted with * are obtained from an independent measurement of the bare resonator and used as fixed parameters in the master equation fit.

6 Coulomb interactions in doubly occupied QDs and WM formations

Supplementary Figure 11a presents the expected orbital splitting (Supplementary Eq. (17)) in planar Ge as a function of the QD radius l_{QD} , assuming an effective hole mass of $m_{\text{HH}}^* = 0.057m_e$ [16], where m_e is the free electron mass. The geometry of our device supports a QD radius of $l_{\text{QD}} \sim 70$ nm, from where we estimate the orbital splitting $\hbar\omega_{\text{orb}}$:

$$\hbar\omega_{\text{orb}} = \frac{\hbar^2}{m^*l_{\text{QD}}^2} \sim 70 h \cdot \text{GHz}. \quad (17)$$

The red shaded region in Supplementary Figure 11a illustrates the resonator frequency bandwidth 4 – 8 GHz in our setup which demonstrates that a QD with $l_{\text{QD}} > 200$ nm is needed to decrease the orbital splitting below 8 $h \cdot \text{GHz}$.

While more elaborated calculations such as full-configuration-interaction (FCI) calculation may capture the complete picture of the dynamics of our QD with multi particles, we provide a simplified two-body Hamiltonian (Supplementary Eq. (19)) also considering Coulomb interaction and confinement anisotropy α . For simplicity, we neglect the possible anisotropies of the effective mass in the Hamiltonian:

$$H = H_0(x_1, y_1) + H_0(x_2, y_2) + V_{\text{int}}(x_1 - x_2, y_1 - y_2) \quad (18)$$

$$H_0(x, y) = \frac{p_x^2 + p_y^2}{2m^*} + \frac{m^*\omega_{\text{orb}}^2}{2} \left(x^2 + \frac{y^2}{\alpha^2} \right) \quad (19)$$

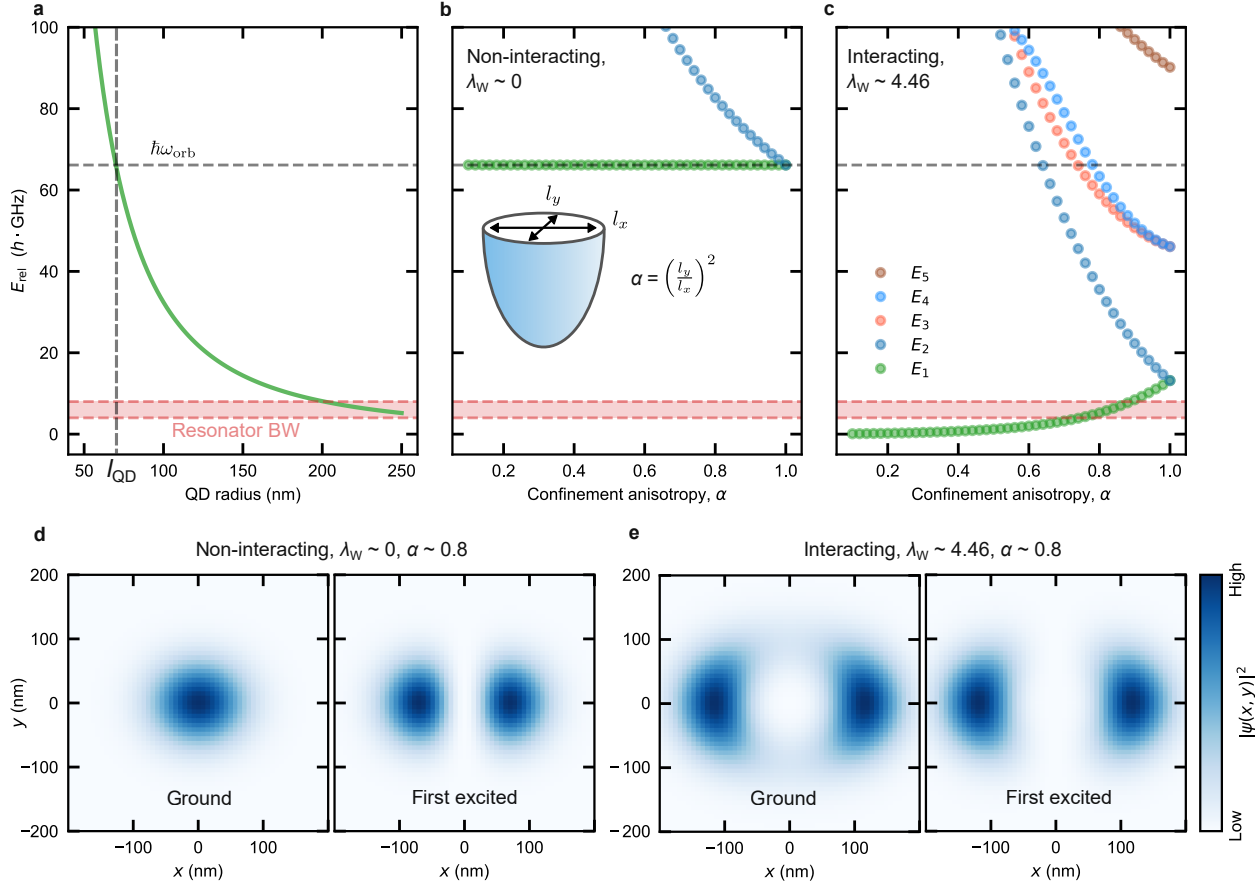
$$V_{\text{int}}(x, y) = \frac{1}{4\pi\epsilon} \frac{e^2}{\sqrt{x^2 + y^2}}. \quad (20)$$

We consider the case with a QD anisotropy $\alpha = (l_y/l_x)^2 \leq 1$ caused by the confinement potential [17], implying that the QD length l_y along the y -axis is shorter than the length l_x along x -axis and thus $\omega_{\text{orb}} \propto 1/l_x^2$. With the electron-electron interaction energy $E_{ee} = e^2/4\pi\epsilon l_x$ given by the Coulomb interaction between two particles separated by l_x , the Wigner ratio $\lambda_W = E_{ee}/\hbar\omega_{\text{orb}} \propto l_x$ quantifies the ratio between Coulomb interaction and confinement potential. Here, we note $\lambda_W \sim 4.46$ is estimated from our QD radius ~ 70 nm.

To study the dependence of the energy scale on α , we separate the full Hamiltonian Supplementary Eq. (19) in the center of mass (COM) coordinate $\mathbf{R} = (\mathbf{r}_1 + \mathbf{r}_2)/\sqrt{2}$ and the relative coordinate $\mathbf{r} = (\mathbf{r}_1 - \mathbf{r}_2)/\sqrt{2}$ with $\mathbf{r}_i = (x_i, y_i)$, as well as $x = x_1 - x_2$ and $y = y_1 - y_2$. This allows the Hamiltonian to be described by $H = H_{\mathbf{R}} + H_{\text{rel}}$ where $H_{\mathbf{R}}$ is the non-interacting 2D harmonic oscillator Hamiltonian in the COM coordinate [18] and H_{rel} is the Hamiltonian in the relative coordinate. We note that while the method of COM and relative coordinates well describes the dynamics of a harmonic single QD, elaborated models such as two-center-oscillator (TCO) may provide more precise description of the dynamics in a DQD [19]. By rescaling l_x to $\tilde{x} = x/l_x$ and $\tilde{y} = y/l_x$, we find

$$\frac{H_{\text{rel}}}{\hbar\omega_{\text{orb}}} = \frac{\tilde{p}_x^2 + \tilde{p}_y^2}{2} + \frac{\tilde{x}^2 + \tilde{y}^2/\alpha^2}{2} + \frac{\lambda_W}{\sqrt{\tilde{x}^2 + \tilde{y}^2}}. \quad (21)$$

Because H_{rel} can capture the physics of strongly-correlated states, we numerically diagonalize Supplementary Eq. (21) to obtain the eigenenergies E_{rel} as a function of α in Supplementary Figures 11b and c. The total energy of the DQD system is then given by $E_{\text{tot}} = E_{\text{rel}} + E_{\mathbf{R}} = E_{\text{rel}} + \hbar\omega_{\text{orb}}m$, with integer m . Supplementary Figure 11b (c) demonstrates the orbital splitting as a function of α with $\lambda_W \sim 0$ (4.46) which represents the non-interacting (interacting) case resulting from Supplementary Eq. (21). Apparently, finite Coulomb interaction quenches down the singlet-triplet splitting (green dots in Supplementary Figures 11b and c) from $\sim 70 h \cdot \text{GHz}$ to $\sim 14 h \cdot \text{GHz}$ in the perfectly anisotropic case ($\alpha = 1$). Additionally for $\alpha < 1$, the singlet-triplet splitting decreases further down in energy only in the interacting case (Supplementary Figure 11c) where we find $\alpha \sim 0.8$ is required to have the excited orbital state within the resonator bandwidth in this two-body model. Furthermore, we also present the effect of Coulomb correlation and confinement anisotropy in the shape of the ground and excited state charge density in Supplementary Figures 11d and e. In the interacting case (Supplementary Figure 11e), the ground state charge density (left panel) becomes similar to that of the excited state (right panel) which is often referred to as a Wigner molecule [18–22]. While the Coulomb interaction and QD confinement anisotropy may have different implications in the specific charge density of the multi-hole QD ground state, our calculation indicates that the orbital state renormalization driven by Coulomb correlation and QD anisotropy results in the low-lying states observed in Fig. 5 and 6.



Supplementary Figure 11 Orbital state renormalization due to Coulomb interaction and confinement anisotropy. **a**, Orbital energy splitting E_1 between ground and first excited state without Coulomb correlation effect as a function of the hole quantum dot (QD) radius. $l_{\text{QD}} \sim 70$ nm denotes the radius of the QD in this work, with the corresponding $\omega_{\text{orb}}/2\pi \sim 70$ GHz. The red shaded region denotes the frequency bandwidth of our resonator 4 – 8 GHz. An effective hole mass of $m^* \sim 0.057m_e$ is assumed, with m_e being the free electron mass. **b** (**c**), E_{rel} as a function of confinement anisotropy α without (with) finite Coulomb correlation effect. A schematic of the confinement potential is shown in **b**, where l_x (l_y) denotes the characteristic length scale of the confinement along the major (minor) axis with $\alpha = (l_y/l_x)^2 \leq 1$. The Wigner ratio $\lambda_W = E_{ee}/\hbar\omega_{\text{orb}}$ quantifies the electron-electron interaction energy with respect to confinement energy. In **c**, $\lambda_W = 4.46$ corresponds to the expected Wigner ratio in our QD. E_1 (green dots) represents the minimal orbital splitting of the QD corresponding to $l_x > l_y$. **d** (**e**), Charge density function spanned around the center of a QD for non-interacting (interacting) case with $\alpha \sim 0.8$. Driven by Coulomb correlation, the ground state charge density (left panel in **e**) becomes similar to that of the excited state (right panel in **e**).

7 Input-output theory for strongly-correlated states

As shown in Figs. 5, 6 and in the Hamiltonian in Methods section, the strongly-correlated states (SCSs) show a multi-level structure. Thereby, a generalization of Supplementary Eq. (16) is required to derive the resonator response and reproduce the observations. Following the derivation from Ref. [23], we first describe the interaction Hamiltonian between the multi-level QDs and the microwave photons, where the resonator effectively couples to the DQD detuning ε as shown below Supplementary Eq. (22). It should be noted that the same interaction Hamiltonian can be utilized for both the even and the odd configuration reported in Fig. 6, because ε couples to the Hamiltonian via τ_z , which is the dipole moment operator in the position basis $[|L_g\rangle, |L_e\rangle, |R_g\rangle, |R_e\rangle]$, where L (R) denotes the charge state with the excess hole in the left (right) QD (see Methods).

$$\begin{aligned}
 H_{\text{int}} &= g_0 \tau_z (a + a^\dagger) \\
 &= g_0 \begin{bmatrix} 1 & 0 & 0 & 0 \\ 0 & \eta_L & 0 & 0 \\ 0 & 0 & -1 & 0 \\ 0 & 0 & 0 & -\eta_R \end{bmatrix} (a + a^\dagger).
 \end{aligned} \tag{22}$$

Here, η_L and η_R account for the different lever-arms of the excited orbital states as discussed in the Methods section. Based on H_{int} we use the input-output theory to simulate the normalized feedline transmission amplitude

$|A/A_0|^2$ shown in Fig. 5b, and in Supplementary Figure 15 for both odd and even cases. The transmission of the hanged-style resonator coupled to multi-level QDs can be written as:

$$S_{21} = |A/A_0| = \frac{\Delta_r - i\kappa_{\text{int}}/2 + g_0 \sum_{n,m} d_{nm}\chi_{nm}}{\Delta_r - i\kappa/2 + g_0 \sum_{n,m} d_{nm}\chi_{nm}}, \quad (23)$$

where the dipole moment operator d and the charge susceptibility χ are matrices to account for different state transitions. The dipole moment operator d can be evaluated by transforming τ_z from the position basis $[|L_g\rangle, |L_e\rangle, |R_g\rangle, |R_e\rangle]$ to the ‘qudit’ basis which diagonalizes the multi-level Hamiltonian (shown in Methods):

$$H_{\text{SCS,diag}} = U_0 H_{\text{SCS}} U_0^\dagger = \sum_{m,n=0}^3 E_n |n\rangle\langle n|, \quad (24)$$

$$d = U_0 \tau_z U_0^\dagger = \sum_{m,n=0}^3 d_{mn} |m\rangle\langle n|, \quad (25)$$

where U_0 is a unitary transformation which diagonalizes H_{SCS} , E_n ($|n\rangle$) are the eigenenergies (eigenstates) of $H_{\text{SCS,diag}}$, $d_{nm} = d_{mn}^*$ are the matrix elements of d .

The matrix elements of χ can be written as:

$$\chi_{nm} = \frac{g_0 d_{nm} (\rho_m - \rho_n)}{-(E_n/\hbar - E_m/\hbar - \omega_d) + i\gamma_{nm}}, \quad (26)$$

with $\gamma_{nm} = \Gamma_{nm}^\varphi + \Gamma_{nm}^r/2$ representing the total loss rate given by the dephasing (relaxation) rate Γ_{nm}^φ (Γ_{nm}^r) between n and m states. In Supplementary Eq. (26), and $\rho_i \propto e^{-E_i/(k_B T)}$ is the normalized Boltzmann distribution. Since the quantum states are far detuned below the Fermi-level, we assume $T = 10$ mK $\ll T_e$.

To treat the decoherence matrix γ , we introduce the noise Hamiltonian H_n Supplementary Eq. (27) in the position basis [24]:

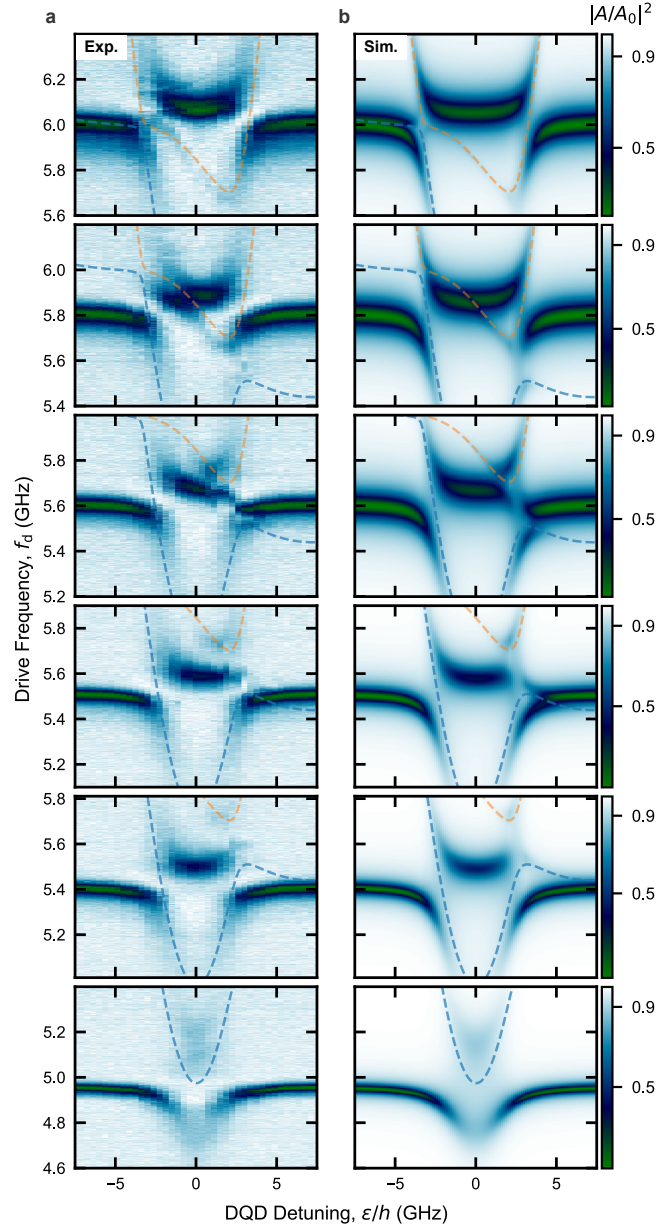
$$\begin{aligned} H_n &= N_\varepsilon + \sum_{i,j} N_{ij} \\ N_\varepsilon &= \xi_\varepsilon \tau_z \\ N_{ij} &= \xi_{ij} (|i\rangle\langle j| + |j\rangle\langle i|). \end{aligned} \quad (27)$$

Here N_ε (N_{ij}) illustrates the noise Hamiltonian with ξ_ε (ξ_{ij}) representing randomly fluctuating noise with the corresponding power spectra $P_\varepsilon(\omega)$ ($P_{ij}(\omega)$). For instance, when $\varepsilon \gg 0$, the qudit basis describes decoupled QDs in the position basis, and $P_{ij}(\omega_i - \omega_j) \propto \Gamma_{ij}^{b,r}$ holds [24], where $\omega_i = E_i/\hbar$ and $\Gamma_{ij}^{b,r}$ is the relaxation rate of the bare quantum state from $|i\rangle$ to $|j\rangle$. In the qudit basis, we interpret $\bar{N}_{nm}^2 \propto \Gamma_{nm}^r$ and $(\bar{N}_{nn} - \bar{N}_{mm})^2 \propto \Gamma_{nm}^\varphi$, with \bar{N} representing the noise Hamiltonian in the qudit basis. We also assume that the low-frequency noise affects the detuning noise, i.e. $P_\varepsilon(0) \sim \Gamma_\varepsilon$ [24]. For the simulations shown in Fig. 5b and Supplementary Figure 15, we empirically use the decoherence parameters of the individual QDs in the position basis shown in Supplementary Table 3. We note, however, that experiments such as the free-induction-decay [25] or relaxation time measurement [26] are required to accurately determine the decoherence parameters.

Parameter	Fig. 5 (MHz)	Supplementary Figure 15a (MHz)	Supplementary Figure 15b (MHz)
$\Gamma_\varepsilon/2\pi$	180	160	180
$\Gamma_{12}^{b,r}/2\pi$	1	1	1
$\Gamma_{34}^{b,r}/2\pi$	1	1	1
$\Gamma_{13}^{b,r}/2\pi$	1	1	1
$\Gamma_{14}^{b,r}/2\pi$	1	1	1
$\Gamma_{24}^{b,r}/2\pi$	30	10	1
$\Gamma_{23}^{b,r}/2\pi$	1	90	1

Supplementary Table 3 Qudit decoherence matrix utilized for the numerical simulations shown in Fig. 5 and Supplementary Figure 15.

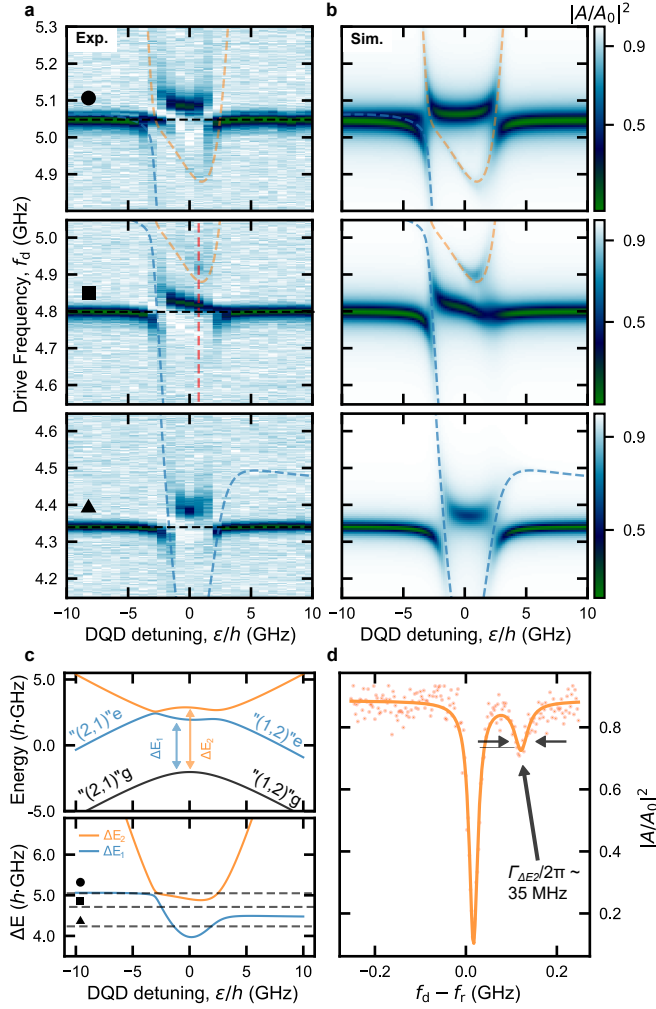
8 Spectroscopies of the strongly-correlated states



Supplementary Figure 12 Detailed spectroscopy of the SCS. **a**, Detailed normalized amplitude of feedline transmission $|A/A_0|^2$ as a function of drive frequency f_d and DQD detuning ε , obtained in correspondence of six different resonator frequencies f_r and for the same inter-dot transition shown in Fig. 5. Blue and orange dashed lines (identical to the ones shown in Fig. 5) correspond to the first and second excited spectrum in the presence of the quenched SCS. **b**, Simulation of $|A/A_0|^2$ obtained by the multi-level DQD input-output theory. The parameters used for the simulations are reported in Supplementary Table 4.

Parameter	Fig. 5 ($h \cdot \text{GHz}$)
Δ_L	5.40
Δ_R	4.73
t_{11}	2.49
t_{12}	0.21
t_{21}	0.11
t_{22}	1.69
$\hbar g_0$	0.22

Supplementary Table 4 SCS Hamiltonian parameters (see Eq. (2) in Methods) reproducing the experimental data reported in Fig. 5a, and Supplementary Figure 12. The resonator parameters, including κ_{int} and κ , are extracted from Fig. 1g in correspondence of the f_r used in the different panels.

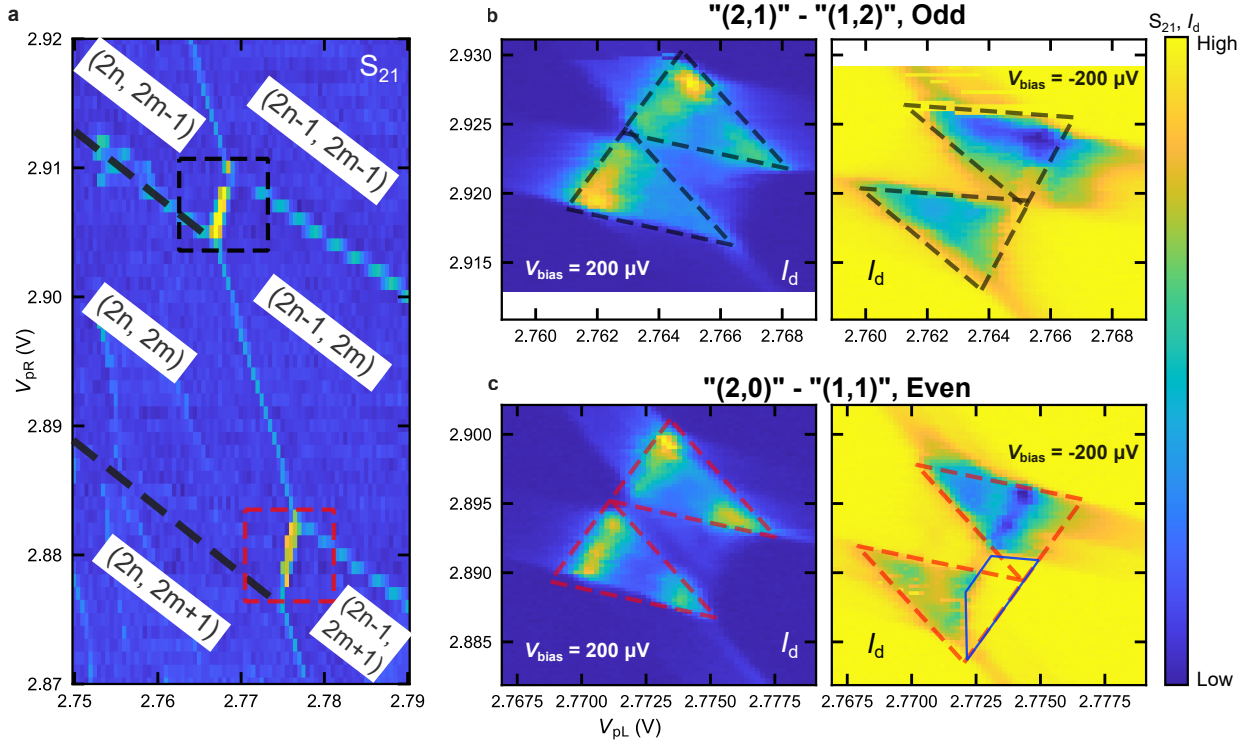


Supplementary Figure 13 SCS spectroscopy in a different electrostatic configuration. **a**, Normalized amplitude of feedline transmission $|A/A_0|^2$ as a function of drive frequency f_d and DQD detuning ε for three different resonator frequencies f_r . An inter-dot transition different from the one investigated in Fig. 5 is studied here. **b**, Simulated $|A/A_0|^2$ for the three different f_r in **a**, using a generalized input-output theory for multi-level DQD systems (see Methods, and Supplementary Note 7). The relevant parameters are shown in Supplementary Table 5. **c**, Energy-level diagram (top panel) and excitation energy Δ_E (bottom panel) calculated with the 4×4 Hamiltonian in Methods, and used for the input-output simulation in **b**. Bottom panel: Blue (orange) curve corresponds to the energy spitting ΔE_1 (ΔE_2) between the first (second) excited state and the ground state shown in the upper panel. ΔE_1 (ΔE_2) spectrum is superimposed to **a** and **b** in blue (orange) dashed line. **d**, Line-cut along the red dashed line shown in the middle panel of **a**. A fit to a Lorentzian model results in $\Gamma_{\Delta E_2}/2\pi \sim 35$ MHz.

Parameter	Value ($h \cdot \text{GHz}$)
Δ_L	5.03
Δ_R	4.45
t_{11}	2.00
t_{12}	0.50
t_{21}	0.22
t_{22}	1.90
hg_0	0.13

Supplementary Table 5 SCS Hamiltonian parameters (see Eq. (2) in Methods) reproducing the experimental data reported in Supplementary Figure 13. The resonator parameters, including κ_{int} and κ , are extracted from Fig. 1g in correspondence to the f_r used in the different panels.

9 DC transport measurements in the even and odd hole configurations



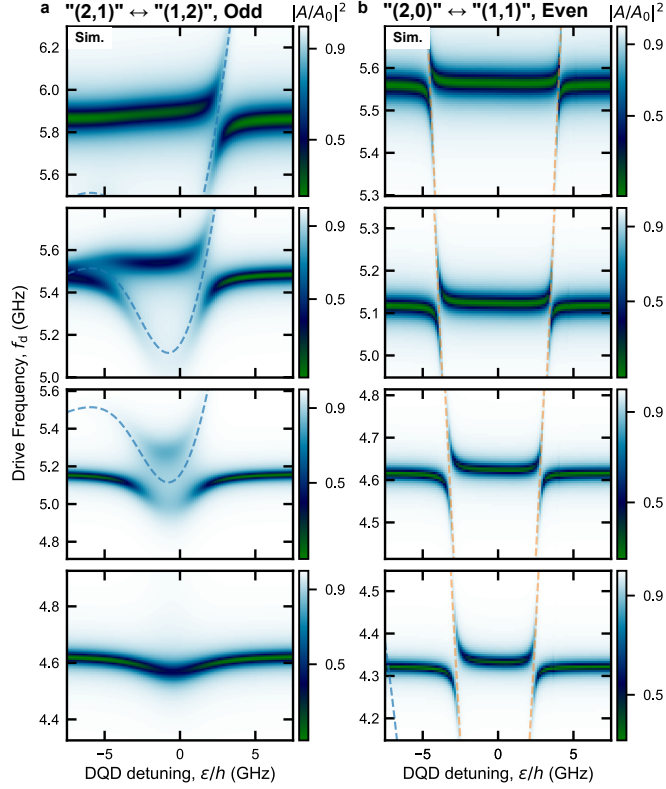
Supplementary Figure 14 DC bias triangle measurements in the even and odd total hole number configurations. **a**, Stability diagram spanned by V_{pL} and V_{pR} showing two adjacent inter-dot transitions. Amplitude of the feedline transmission S_{21} is recorded. (p, q) denotes the relevant charge configuration where p (q) is the hole number in the left (right) QD. **b**, Bias-triangle measurements at the $(2n, 2m-1) \leftrightarrow (2n-1, 2m)$ (“(2,1)” \leftrightarrow “(1,2)”) inter-dot transition (black-dashed box in **a**), corresponding to the one investigated in Fig. 6a. The dc-current through the DQD, I_d , is recorded. Left (right) panel shows the bias-triangle measured with $V_{\text{bias}} = 200 \mu\text{V}$ ($-200 \mu\text{V}$). The black-dashed triangles with the same shape and size are superimposed to the both panels, showing no indication of the Pauli spin blockade (PSB). **c**, The same measurement as in **b** at the $(2n, 2m) \leftrightarrow (2n-1, 2m+1)$ (“(2,0)” \leftrightarrow “(1,1)”) inter-dot transition (red-dashed box in **a**) corresponding to the one investigated in Fig. 6b. The red-dashed triangles with the same shape and size are superimposed to the both panels, where in the right panel, the possible indication of the PSB is denoted by the blue trapezoid.

Two adjacent inter-dot transitions corresponding to those investigated with the resonator in Fig. 6 were characterized through dc-transport measurements. Supplementary Figure 14a displays these transitions in terms of the feedline transmission amplitude, S_{21} , as a function of V_{pR} and V_{pL} . When a finite bias voltage, V_{bias} , is applied at the source ohmic contact, bias triangles near the triple points in the charge stability diagrams emerge [27, 28], as shown in Supplementary Figure 14b. The left panel represents the bias triangles measured under $V_{\text{bias}} = +200 \mu\text{V}$, while the right panel corresponds to $V_{\text{bias}} = -200 \mu\text{V}$, both at the $(2n, 2m-1) \leftrightarrow (2n-1, 2m)$

“(2, 1)” \leftrightarrow “(1, 2)” inter-dot transition, as denoted by the odd, black dashed box in Supplementary Figure 14a. To facilitate a comparison of the bias triangles, superimposed black dashed triangles of the same size but with different orientations were included in Supplementary Figure 14b. When the size of the bias triangles closely matches, it implies no indication of the Pauli spin blockade (PSB).

In contrast, Supplementary Figure 14c depicts the same measurement as in Supplementary Figure 14b but at the $(2n, 2m) \leftrightarrow (2n-1, 2m+1)$ (“(2, 0)” \leftrightarrow “(1, 1)”) inter-dot transition (even configuration, red dashed box in Supplementary Figure 14a), corresponding to the one investigated in Fig. 6b. In this case, representing the even scenario, the size of the bias triangles (red dashed triangles in Supplementary Figure 14c) measured with the opposite polarity of V_{bias} does not match, revealing a region where the current is blocked (blue trapezoid in the right panel). While more detailed studies, including the introduction of a finite magnetic field [29], are required to undeniably confirm this observation, the observed current blockade presents a potential indication of the Pauli spin blockade (PSB). The PSB is expected for inter-dot transitions with a total even number of particles [27]. From the width of the PSB region in the DQD bias triangles, we extract an orbital splitting of $\sim 7.8 \pm 1.2 h \cdot \text{GHz}$ (where the error is determined by the size of voltage step utilized in Supplementary Figure 14c), which aligns with the estimated $\Delta_L \sim 5.46 h \cdot \text{GHz}$ in Fig. 6a, providing further support for the presence of strongly-correlated states in this study.

10 Simulations of spectroscopies in Fig. 6



Supplementary Figure 15 Simulation of the resonator spectra shown in Fig. 6. Simulated normalized amplitude of feedline transmission $|A/A_0|^2$ of the corresponding measurements in Fig. 6, using an extended master equation model of the multi-level DQD system (see Methods and Supplementary Note 7) for an odd (a, see Fig. 6a) and an even (b, see Fig. 6b) DQD configuration, respectively. Relevant parameters for the simulations are reported in Supplementary Table 6, which are also used for calculating the energy level diagram and the excitation energy spectra shown in Fig. 6e and f. The observed asymmetry in ε of Fig. 6a, as already in Fig. 5, signals the presence of an additional excited state associated with a SCS. This results in an excitation energy around $\sim 5 h \cdot \text{GHz}$ for the left QD, while the excited state of the right QD cannot be resolved up to $f_r \sim 6.3 \text{ GHz}$. The observed asymmetry in ε , as shown in Fig. 6a, signals the presence of an additional excited state associated with a SCS around $\sim 5 h \cdot \text{GHz}$ in the left QD.

Parameter	Fig. 6a, Odd ($h \cdot \text{GHz}$)	Fig. 6b, Even ($h \cdot \text{GHz}$)
Δ_L	5.48	5.48
Δ_R	6.50*	0.00
t_{11}	2.65	1.60
t_{12}	0.30*	0.00
t_{21}	1.25	0.00
t_{22}	1.70*	2.20
hg_0	0.19	0.12

Supplementary Table 6 SCS Hamiltonian parameters reproducing the experimental data reported in Fig. 6a, and b. The resonator parameters including κ_{int} and κ are extracted from Fig. 1g in correspondence to the f_r used in the different panels. For this specific DQD configuration, the parameters indicated by * are the arbitrary values which cannot be determined from the measurement in Fig. 6a and do not impact the results of the simulations (see caption of Supplementary Figure 15).

Supplementary References

- [1] Marcus, C.M., Folk, J.A., Patel, S.R., Cronenwett, S.M., Huibers, A.G., Campman, K., Gossard, A.C.: Mesoscopic fluctuations of tunneling and cotunneling in quantum dots. *Superlattices and Microstructures* **23**(1), 161–172 (1998) <https://doi.org/10.1006/spmi.1996.0200>
- [2] Lodari, M., Hendrickx, N.W., Lawrie, W.I.L., Hsiao, T.-K., Vandersypen, L.M.K., Sammak, A., Veldhorst, M., Scappucci, G.: Low percolation density and charge noise with holes in germanium. *Mater. Quantum. Technol.* **1**(1), 011002 (2021) <https://doi.org/10.1088/2633-4356/abcd82>
- [3] Sammak, A., Sabbagh, D., Hendrickx, N.W., Lodari, M., Paquelet Wuetz, B., Tosato, A., Yeoh, L., Bollani, M., Virgilio, M., Schubert, M.A., Zaumseil, P., Capellini, G., Veldhorst, M., Scappucci, G.: Shallow and undoped germanium quantum wells: A playground for spin and hybrid quantum technology. *Advanced Functional Materials* **29**(14), 1807613 (2019) <https://doi.org/10.1002/adfm.201807613> <https://onlinelibrary.wiley.com/doi/pdf/10.1002/adfm.201807613>
- [4] Tracy, L.A., Hwang, E.H., Eng, K., Ten Eyck, G.A., Nordberg, E.P., Childs, K., Carroll, M.S., Lilly, M.P., Das Sarma, S.: Observation of percolation-induced two-dimensional metal-insulator transition in a Si MOSFET. *Phys. Rev. B* **79**(23), 235307 (2009) <https://doi.org/10.1103/PhysRevB.79.235307>
- [5] Kim, J.-S., Tyryshkin, A.M., Lyon, S.A.: Annealing shallow Si/SiO₂ interface traps in electron-beam irradiated high-mobility metal-oxide-silicon transistors. *Applied Physics Letters* **110**(12), 123505 (2017) <https://doi.org/10.1063/1.4979035>
- [6] Mi, X., Hazard, T.M., Payette, C., Wang, K., Zajac, D.M., Cady, J.V., Petta, J.R.: Magnetotransport studies of mobility limiting mechanisms in undoped Si/SiGe heterostructures. *Phys. Rev. B* **92**(3), 035304 (2015) <https://doi.org/10.1103/PhysRevB.92.035304>
- [7] Wiel, W.G., De Franceschi, S., Elzerman, J.M., Fujisawa, T., Tarucha, S., Kouwenhoven, L.P.: Electron transport through double quantum dots. *Rev. Mod. Phys.* **75**, 1–22 (2002) <https://doi.org/10.1103/RevModPhys.75.1>
- [8] Frey, T., Leek, P.J., Beck, M., Faist, J., Wallraff, A., Ensslin, K., Ihn, T., Büttiker, M.: Quantum dot admittance probed at microwave frequencies with an on-chip resonator. *Phys. Rev. B* **86**(11), 115303 (2012) <https://doi.org/10.1103/PhysRevB.86.115303>
- [9] Göppl, M., Fagner, A., Baur, M., Bianchetti, R., Filipp, S., Fink, J.M., Leek, P.J., Puebla, G., Steffen, L., Wallraff, A.: Coplanar waveguide resonators for circuit quantum electrodynamics. *Journal of Applied Physics* **104**(11), 113904 (2008) <https://doi.org/10.1063/1.3010859>
- [10] Ambegaokar, V., Baratoff, A.: Tunneling Between Superconductors. *Physical Review Letters* **10**(11), 486–489 (1963) <https://doi.org/10.1103/PhysRevLett.10.486>
- [11] Blais, A., Grimsmo, A.L., Girvin, S.M., Wallraff, A.: Circuit quantum electrodynamics. *Reviews of Modern Physics* **93**(2), 025005 (2021) <https://doi.org/10.1103/RevModPhys.93.025005>
- [12] Müller, C., Cole, J.H., Lisenfeld, J.: Towards understanding two-level-systems in amorphous solids: insights from quantum circuits. *Reports on Progress in Physics* **82**(12), 124501 (2019) <https://doi.org/10.1088/1361-6633/ab3a7e>
- [13] Collett, M.J., Gardiner, C.W.: Squeezing of intracavity and traveling-wave light fields produced in parametric amplification. *Phys. Rev. A* **30**, 1386–1391 (1984) <https://doi.org/10.1103/PhysRevA.30.1386>
- [14] Chen, Q.-M., Partanen, M., Fesquet, F., Honasoge, K.E., Kronowetter, F., Nojiri, Y., Renger, M., Fedorov, K.G., Marx, A., Deppe, F., Gross, R.: Scattering coefficients of superconducting microwave resonators. ii. system-bath approach. *Phys. Rev. B* **106**, 214506 (2022) <https://doi.org/10.1103/PhysRevB.106.214506>
- [15] Probst, S., Song, F.B., Bushev, P.A., Ustinov, A.V., Weides, M.: Efficient and robust analysis of complex scattering data under noise in microwave resonators. *Review of Scientific Instruments* **86**(2) (2015) <https://doi.org/10.1063/1.4907935>
- [16] Scappucci, G., Kloeffel, C., Zwanenburg, F.A., Loss, D., Myronov, M., Zhang, J.-J., De Franceschi, S., Katsaros, G., Veldhorst, M.: The germanium quantum information route. *Nat Rev Mater* **6**(10), 926–943

(2021) <https://doi.org/10.1038/s41578-020-00262-z>

- [17] Drouvelis, P.S., Schmelcher, P., Diakonov, F.K.: Global view on the electronic properties of two-electron anisotropic quantum dots. *Physical Review B* **69**(3), 035333 (2004) <https://doi.org/10.1103/PhysRevB.69.035333>
- [18] Abadillo-Uriel, J.C., Martinez, B., Filippone, M., Niquet, Y.-M.: Two-body Wigner molecularization in asymmetric quantum dot spin qubits. *Phys. Rev. B* **104**(19), 195305 (2021) <https://doi.org/10.1103/PhysRevB.104.195305>
- [19] Yannouleas, C., Landman, U.: Molecular formations and spectra due to electron correlations in three-electron hybrid double-well qubits. *Phys. Rev. B* **105**(20), 205302 (2022) <https://doi.org/10.1103/PhysRevB.105.205302>
- [20] Yannouleas, C., Landman, U.: Spontaneous Symmetry Breaking in Single and Molecular Quantum Dots. *Physical Review Letters* **82**(26), 5325–5328 (1999) <https://doi.org/10.1103/PhysRevLett.82.5325>
- [21] Li, Y., Yannouleas, C., Landman, U.: Artificial quantum-dot helium molecules: Electronic spectra, spin structures, and Heisenberg clusters. *Physical Review B* **80**(4), 045326 (2009) <https://doi.org/10.1103/PhysRevB.80.045326>
- [22] Yannouleas, C., Landman, U.: Symmetry breaking and quantum correlations in finite systems: Studies of quantum dots and ultracold Bose gases and related nuclear and chemical methods. *Reports on Progress in Physics* **70**(12), 2067 (2007) <https://doi.org/10.1088/0034-4885/70/12/R02>
- [23] Burkard, G., Petta, J.R.: Dispersive readout of valley splittings in cavity-coupled silicon quantum dots. *Physical Review B* **94**(19), 195305 (2016) <https://doi.org/10.1103/PhysRevB.94.195305>
- [24] Stockklauser, A.: Strong Coupling Circuit QED with Semiconductor Quantum Dots. Doctoral Thesis, ETH Zurich (2017). <https://doi.org/10.3929/ethz-b-000259894>
- [25] Dial, O.E., Shulman, M.D., Harvey, S.P., Bluhm, H., Umansky, V., Yacoby, A.: Charge Noise Spectroscopy Using Coherent Exchange Oscillations in a Singlet-Triplet Qubit. *Physical Review Letters* **110**(14), 146804 (2013) <https://doi.org/10.1103/PhysRevLett.110.146804>
- [26] Lawrie, W.I.L., Hendrickx, N.W., van Riggelen, F., Russ, M., Petit, L., Sammak, A., Scappucci, G., Veldhorst, M.: Spin Relaxation Benchmarks and Individual Qubit Addressability for Holes in Quantum Dots. *Nano Letters* **20**(10), 7237–7242 (2020) <https://doi.org/10.1021/acs.nanolett.0c02589>
- [27] Johnson, A.C., Petta, J.R., Marcus, C.M., Hanson, M.P., Gossard, A.C.: Singlet-triplet spin blockade and charge sensing in a few-electron double quantum dot. *Physical Review B* **72**(16), 165308 (2005) <https://doi.org/10.1103/PhysRevB.72.165308>
- [28] Hanson, R., Kouwenhoven, L.P., Petta, J.R., Tarucha, S., Vandersypen, L.M.K.: Spins in few-electron quantum dots. *Rev. Mod. Phys.* **79**(4), 1217–1265 (2007) <https://doi.org/10.1103/RevModPhys.79.1217>
- [29] Shaji, N., Simmons, C.B., Thalakulam, M., Klein, L.J., Qin, H., Luo, H., Savage, D.E., Lagally, M.G., Rimberg, A.J., Joynt, R., Friesen, M., Blick, R.H., Coppersmith, S.N., Eriksson, M.A.: Spin blockade and lifetime-enhanced transport in a few-electron Si/SiGe double quantum dot. *Nature Physics* **4**(7), 540–544 (2008) <https://doi.org/10.1038/nphys988>